

# High-Dimensional Bayesian Likelihood Normalisation for CRESST's Background Model

G. Angloher<sup>1</sup>, S. Banik<sup>2,3</sup>, G. Benato<sup>4</sup>, A. Bento<sup>1,9</sup>, A. Bertolini<sup>1</sup>, R. Breier<sup>5</sup>, C. Bucci<sup>4</sup>, J. Burkhart<sup>a,2</sup>, L. Canonica<sup>1</sup>, A. D'Addabbo<sup>4</sup>, S. Di Lorenzo<sup>4</sup>, L. Einfalt<sup>2,3</sup>, A. Erb<sup>6,10</sup>, F. v. Feilitzsch<sup>6</sup>, S. Fichtinger<sup>2</sup>, D. Fuchs<sup>1</sup>, A. Garai<sup>1</sup>, V.M. Ghete<sup>2</sup>, P. Gorla<sup>4</sup>, P.V. Guillaumon<sup>4</sup>, S. Gupta<sup>2</sup>, D. Hauff<sup>1</sup>, M. Jeřkovský<sup>5</sup>, J. Jochum<sup>7</sup>, M. Kaznacheeva<sup>6</sup>, A. Kinast<sup>6</sup>, H. Kluck<sup>b,2</sup>, H. Kraus<sup>8</sup>, S. Kuckuk<sup>7</sup>, A. Langenkämper<sup>1</sup>, M. Mancuso<sup>1</sup>, L. Marini<sup>4,11</sup>, L. Meyer<sup>7</sup>, V. Mokina<sup>c,2</sup>, A. Nilima<sup>1</sup>, M. Olmi<sup>4</sup>, T. Ortmann<sup>6</sup>, C. Pagliarone<sup>4,12</sup>, L. Pattavina<sup>4,6</sup>, F. Petricca<sup>1</sup>, W. Potzel<sup>6</sup>, P. Povinec<sup>5</sup>, F. Pröbst<sup>1</sup>, F. Pucci<sup>1</sup>, F. Reindl<sup>2,3</sup>, J. Rothe<sup>6</sup>, K. Schöffner<sup>1</sup>, J. Schieck<sup>2,3</sup>, D. Schmiedmayer<sup>2,3</sup>, S. Schönert<sup>6</sup>, C. Schwertner<sup>2,3</sup>, M. Stahlberg<sup>1</sup>, L. Stodolsky<sup>1</sup>, C. Strandhagen<sup>7</sup>, R. Strauss<sup>6</sup>, I. Usherov<sup>7</sup>, F. Wagner<sup>2</sup>, M. Willers<sup>6</sup>, V. Zema<sup>1</sup> (CRESST Collaboration), F. Ferella<sup>4,13</sup>, M. Laubenstein<sup>4</sup>, S. Nisi<sup>4</sup>

<sup>1</sup>Max-Planck-Institut für Physik, D-80805 München, Germany

<sup>2</sup>Institut für Hochenergiephysik der Österreichischen Akademie der Wissenschaften, A-1050 Wien, Austria

<sup>3</sup>Atominstytut, Technische Universität Wien, A-1020 Wien, Austria

<sup>4</sup>INFN, Laboratori Nazionali del Gran Sasso, I-67100 Assergi, Italy

<sup>5</sup>Comenius University, Faculty of Mathematics, Physics and Informatics, 84248 Bratislava, Slovakia

<sup>6</sup>Physik-Department, Technische Universität München, D-85747 Garching, Germany

<sup>7</sup>Eberhard-Karls-Universität Tübingen, D-72076 Tübingen, Germany

<sup>8</sup>Department of Physics, University of Oxford, Oxford OX1 3RH, United Kingdom

<sup>9</sup>also at: LIBPhys-UC, Departamento de Física, Universidade de Coimbra, P3004 516 Coimbra, Portugal

<sup>10</sup>also at: Walther-Meißner-Institut für Tieftemperaturforschung, D-85748 Garching, Germany

<sup>11</sup>also at: GSSI-Gran Sasso Science Institute, I-67100 L'Aquila, Italy

<sup>12</sup>also at: Dipartimento di Ingegneria Civile e Meccanica, Università degli Studi di Cassino e del Lazio Meridionale, I-03043 Cassino, Italy

<sup>13</sup>also at: Department of Physical and Chemical Sciences, University of L'Aquila, via Vetoio (COPPITO 1-2), I-67100 L'Aquila, Italy

the date of receipt and acceptance should be inserted later

**Abstract** Using CaWO<sub>4</sub> crystals as cryogenic calorimeters, the CRESST experiment searches for nuclear recoils caused by the scattering of potential Dark Matter particles. A reliable identification of a potential signal crucially depends on an accurate background model. In this work we introduce an improved normalisation method for CRESST's model of the electromagnetic backgrounds. Spectral templates, based on Geant4 simulations, are normalised via a Bayesian likelihood fit to experimental background data. Contrary to our previous work, no assumption of partial secular equilibrium is required, which results in a more robust and versatile applicability. Furthermore, considering the correlation between all background components allows us to explain 82.7 % of the experimental background within [1 keV, 40 keV], an improvement of 18.6 % compared to our previous method.

## 1 Introduction

One of the biggest questions in modern physics is the nature of Dark Matter (DM): albeit its effects are established by astronomical observations, no particle candidate could be found so far, see e.g. [1, 2] for a review.

CRESST is one of the leading experiments that searches directly for DM at the sub-GeV $c^{-2}$  mass scale at the Laboratori Nazionali del Gran Sasso (LNGS). The event signature of a potential DM interaction would be a nuclear recoil inside the target caused by the scattering of a DM particle. By default, CRESST operates scintillating CaWO<sub>4</sub> target crystals as cryogenic calorimeters, which can measure the phonon and the light signal on an event-by-event basis. Combining both signal channels enables the differentiation of nuclear recoils from electromagnetic interactions [3]. Assuming classic leptophobic DM (see e.g. [4]), the former may be a potential DM signal, whereas the latter is most likely a background event caused by natural radioactivity inside and outside the target crystal.

<sup>a</sup>Corresponding author: jens.burkhart@oeaw.ac.at

<sup>b</sup>Corresponding author: holger.kluck@oeaw.ac.at

<sup>c</sup>Corresponding author: valentyina.mokina@oeaw.ac.at

Recently, CRESST reached detection thresholds for nuclear recoils as low as 10.0 eV, which allows us to constrain spin-independent and spin-dependent DM interactions down to a DM mass below  $160 \text{ MeV}c^{-2}$  [5]. At such low energy scales, the discrimination power against electromagnetic backgrounds degrades [6] because electromagnetic and nuclear recoil events starts to mix due to decreased energy emission in the light channel. Hence, a detailed and reliable background description and prediction is crucial. Furthermore, it has to be applicable to all of CRESST's detector modules, which are not solely based on  $\text{CaWO}_4$  crystals, but also on other target materials such as  $\text{Al}_2\text{O}_3$  [7],  $\text{LiAlO}_2$  [8, 9] and Si [5].

To describe and predict the background, we use a framework that consists of a background *model* (i.e. a set of *physics* assumptions about the background components, and the strength and location of their sources), the *Monte Carlo* (MC) code Geant4 [10–12] to simulate the background based on the model, and a *normalisation method* for the simulated data (i.e. a set of *technical* rules how to connect the simulated data to the observed data). The focus of this work is to introduce a new normalisation method to CRESST's background framework and to illustrate how this enables an extension of the existing background model [13] by considering additional components. The full realisation of this extended background model and a detailed discussion of its impact on CRESST will be the topic of a future publication. Similarly, this study is limited to energies above 1 keV where the principal nature of the observed background (i.e. intrinsic contaminations or ambient radiation) is known and the principle applicability of Geant4 is given. The Low Energy Excess of unknown origin at the  $O(100 \text{ eV})$  scale [14, 15] and the questions how reliable Geant4 simulations are at sub-keV energies [16] are beyond the scope of this work.

Generally, we normalise the simulation to dedicated screening measurements of the radioactive contaminations and to reference sets of background data recorded with CRESST. Based on this, we established the first fully MC based background model of CRESST in our previous work [13], as well as the following procedure, which we call the *Gaussian fit method* (GFM) hereafter: the background activities are determined from parametric Gaussian fits to clearly visible alpha and gamma lines at sideband-measurements and assume partial *secular equilibrium* (SE) [17] to propagate the obtained activity to beta-decaying radionuclides which deposit energy in the energy *range of interest* (ROI), for details see [13].

However, the degree to which the partial SE is fulfilled for long-lived radionuclides varies between different crystals due to their production spread [18, 19] and cannot be known a priori. To overcome the assumption of partial SE for future target crystals used by the CRESST experiment, we developed an improved normalisation method based on a combined Bayesian likelihood fit of all considered back-

ground components, which we call *likelihood normalisation method* (LNM hereafter).

Besides being a new *normalisation method* with its own advantages, the LNM allows us also to extend the *background model*, i.e. we can consider additional background components in our attempt to explain the observed data, beyond the ones used in [13]. In our previous work and in this work, we assume that the background can be entirely explained by electromagnetic interactions caused by bulk contaminations in the crystal and surrounding copper parts; our previous work indicates that surface contaminations are subdominant. The insignificance of neutron background was proven in a recent study [20]. In this work, we improve the treatment of several background components: the LNM enables us for the first time to incorporate peak-less spectra (e.g.  $^3\text{H}$ ) and spectra which share the same peaks but deviate in their continuous part (e.g.  $^{40}\text{K}$  in different parts of the setup) directly in the fit. As constraints for the LNM, this work incorporates stricter limits on the contamination in the copper parts of the detectors, which could be set through dedicated screening measurements. We note that future extensions of the background model, e.g. including more background components or more precise experimental constraints, may change the predicted background level and composition, but this will not affect the benefits of the LNM that we present here.

Using the TUM40 detector module as a test case, we show the benefits of the LNM (and the improved background model enabled by the LNM) with respect to the previously used GFM (and the original background model limited by the GFM). First physics results of the LNM, i.e. a study on how strict partial SE is present in a  $\text{CaWO}_4$  crystal, were already published in [21].

In section 2, we briefly describe the components of CRESST's background model, including the reference data sets, to provide context for our test case and the benchmark we use for model comparison. Afterwards, we introduce the new LNM in section 3. In section 4, we report the results of the screening measurements, with which we determine some priors for the likelihood. We report the outcome of the LNM in section 5, and subsequently we discuss its performance in comparison to the previous GFM in section 6. Finally, we conclude in section 7. In Appendix A we provide the latest results obtained with the GFM as a baseline for comparison, in Appendix B we summarise the improvements of the current background model used in this work to the original model developed in [13], in Appendix C we give the details of preparation and measurements of the copper samples that lead to the improved contamination limits used in this work, and in Appendix D we report the obtained activities of all background components for both normalisation methods: GFM and LNM.

## 2 CRESST's Background Model

The GFM was described in our previous work [13], where we developed a first fully MC-based model for the electromagnetic background of the CRESST experiment using the TUM40 detector module as an example, see fig. 1 and [13, fig. 6]. To demonstrate the benefits of the LNM over the GFM, we apply the new method also to the TUM40 detector module as our *test case*. Hence, we use a similar set of background sources (section 2.1), the same reference data set (section 2.2), and slightly updated spectral templates (section 2.3). In Appendix B we give the detailed differences between the background model used in this work and the previous work.

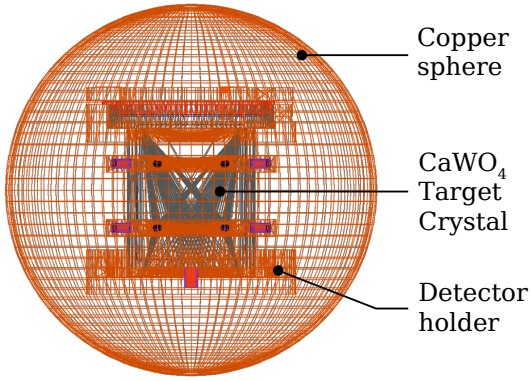


Fig. 1: Visualisation of the TUM40 detector module as implemented in Geant4: 469 g of copper holds 246 g of  $\text{CaWO}_4$  as target, both are encapsulated by a 1mm-thick copper sphere with a mass of 803 g.

### 2.1 Background Sources

Our set of physical background sources is split in four background categories: *internal radiogenic* (IR), *internal cosmogenic* (IC), *near external radiogenic* (NER), and *additional external radiogenic* (AER). All categories are treated as bulk contaminations and no dedicated contribution from surface events are taken into account.

In the background model for the LNM, we omit those radionuclides which turned out to be negligible, either because their Q-value lies outside the range of detectable energies or because their branching ratio is insignificant (see table 7 for details). Furthermore, we use the capability of the LNM to discriminate between templates which share the same peaks but deviate in their continuous parts. This allows us to consider e.g.  $^{40}\text{K}$  as IR and NER background components (see fig. 2). See also fig. 3 as an example where peaks of

different nuclides overlap due to the finite detector resolution (see section 2.3).

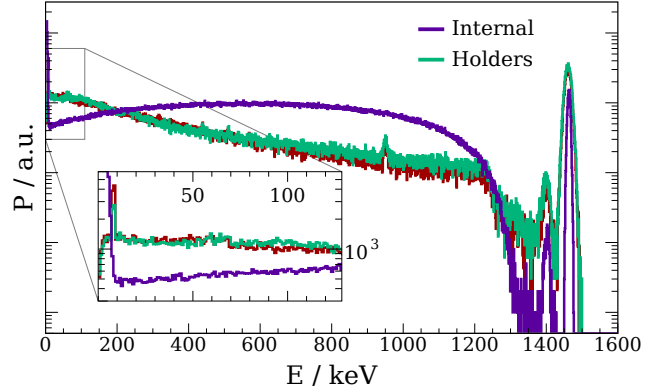


Fig. 2: Comparison of the simulated spectral templates caused by  $^{40}\text{K}$  in the target crystal (*purple*), in the detector holder (*green*), and in the copper shell (*red*). The *inlay* shows a zoom of the energy range until 120 keV. The spectra are normalised to  $10^6$  decays and have a bin width of 1 keV.

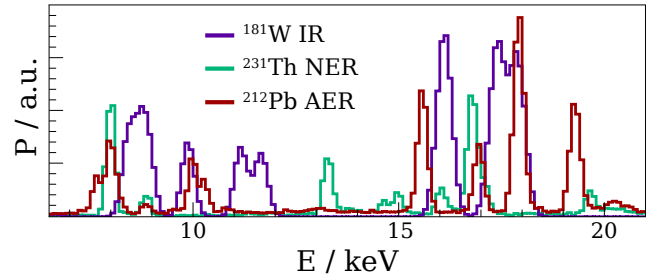


Fig. 3: Simulated spectral templates caused by  $^{181}\text{W}$  in the target crystal (*purple*),  $^{231}\text{Th}$  in the detector holder (*green*), and  $^{212}\text{Pb}$  in the copper shell (*red*) in a part of the energy range of interest. The normalisation values are arbitrary and the bin width is 1 keV.

For the IR background we consider by the natural contamination of the  $\text{CaWO}_4$  crystals with  $^{40}\text{K}$  and the 46 radionuclides from the three radioactive decay chains of  $^{232}\text{Th}$ ,  $^{235}\text{U}$ , and  $^{238}\text{U}$ . As ten of these nuclides are dispensable, see table 7, we consider in total 36 components for IR.

The IC background is caused by the activation of the target crystal due to its exposure to cosmic rays during production. Only decays of  $^3\text{H}$ ,  $^{179}\text{Ta}$ , and  $^{181}\text{W}$  are considered. Due to the capability of the LNM to process also featureless, pure beta spectra, the  $^3\text{H}$  activity can be determined directly from the reference data. We split the contributions of  $^{179}\text{Ta}$  caused by electron capture (EC) into individual templates according to the involved atomic shells because the used Geant4 version (see 2.3) wrongly assigns equal capture probabilities

regardless of the captured electron's shell of origin. With the capability of the LNM to treat also strongly overlapping peaks, we can disentangle the M-shells. This gives a total number of nine IC components.

The NER background is caused by the radioactive contamination of the detector housing, which is made of NOSV copper (see section 4) and surrounds the crystal. In this work, we consider a subset of 28 out of 46 radionuclides from the three natural decay chains (see table 7), and assume no SE at all. Together with  $^{40}\text{K}$ , this makes in total 29 components in the NER category.

Finally, the AER background consists of ten observed nuclides whose activities cannot be completely explained by the IR, IC, and NER background components:  $^{40}\text{K}$ ,  $^{208}\text{Tl}$ ,  $^{210}\text{Pb}$ ,  $^{212}\text{Pb}$ ,  $^{212}\text{Bi}$ ,  $^{214}\text{Bi}$ ,  $^{226}\text{Ra}$ ,  $^{228}\text{Ac}$ ,  $^{234}\text{Th}$ , and  $^{228}\text{Ra}$ . The latter is added in an attempt to explain a yet unidentified peak at 13 keV, see section 6. It is assumed that these components originate outside the detector module, in e.g. the copper parts of the cryostat or the copper shields of CRESST's setup. As the precise origin is unknown, we approximate the exact geometry of the setup with an arbitrary 1 mm-thick copper sphere around the detector module, see fig. 1.

## 2.2 Reference Data Set

For the normalisation we use data from the detector module TUM40 as experimental *reference data* and the same ROI ([1 keV, 40 keV]) as was used in the Dark Matter analysis of TUM40 [22]. Due to the peculiarities of CRESST's event reconstruction, the same data are analysed in three different ways, resulting in three data sets  $D_j$  which are tuned to and identified by the energy range  $E_j$  they cover: *low*  $E_l = [0.6 \text{ keV}, 495 \text{ keV}]$ , *medium*  $E_m = [511 \text{ keV}, 2800 \text{ keV}]$ , and *high*  $E_h = [4 \text{ MeV}, 7 \text{ MeV}]$  with the *data set index*  $j = \{l, m, h\}$ . The collected gross exposure is the same for all data sets since target mass and *live-time*  $T = 523.8 \text{ d}$  are identical.

Each set has its own *signal survival probability* (SSP)  $\varepsilon_{\text{SSP},j}(E)$  which is independent of the decay process and specific to the experimental setup and the applied event reconstruction, see [13] for details. Pile-up events caused by fast, subsequent decays of  $^{212}\text{Bi} \rightarrow ^{212}\text{Po}$ ,  $^{214}\text{Bi} \rightarrow ^{214}\text{Po}$  and  $^{219}\text{Rn} \rightarrow ^{215}\text{Po}$ , which were observed in [23], are excluded from the reference data by the applied quality cuts [24] and hence are not considered in the background model.

## 2.3 Simulated Background Spectra

We reuse the simulations of individual background components, which were produced for our previous work with the ImpCRESST physics simulation code [13] based on Geant4 version 10.2 patch 1. To create *spectral templates*  $T_{VXi}$  we apply the following procedure (see [13] for details): (i) in the

simulation at time  $t = 0$  we place  $N_{VX,0}$  nuclei of type  $X$  in their respective parent volume  $V$  (the  $\text{CaWO}_4$  crystal for IR and IC, the copper detector module for NER, the copper sphere for AER); (ii) let them decay but stop the decay after a ground state is reached; (iii) propagate the decay products to the  $\text{CaWO}_4$  crystal; (iv) record the energy deposited in the target crystal  $E_{\text{dep}}$ ; (v) apply the empirical energy and time resolution of the TUM40 detector module to get the observed energy spectrum  $E$ ; compared to our previous work we apply an improved parameterisation of the empirical energy resolution, which leads to a better match between observed and simulated peak widths in our medium energy data set; (vi) count the *simulated entries*  $\tilde{n}_i$  in the  $i$ -th energy bin  $E_i$ .

Finally, the spectral template is given as

$$\begin{aligned} T_{VXi} &= \frac{\sum_i \tilde{n}_i(E_i)}{N_{VX,0}} \cdot \frac{\tilde{n}_i(E_i)}{\sum_i \tilde{n}_i(E_i)} \\ &= \varepsilon_{g,VX} \cdot f_{VXi}(E_i), \end{aligned} \quad (1)$$

where  $f_{VXi} = \tilde{n}_i(E_i)/\sum_i \tilde{n}_i(E_i)$  is an empiric *probability density function* (PDF), i.e. the probability that an energy deposition in the target by nuclide  $X$  in source volume  $V$  falls in energy bin  $i$ , normalised to unity. The *geometric efficiency*  $\varepsilon_{g,VX}$  is the ratio of particles that deposit energy in the target over all decays of contaminant  $X$  at the source, i.e. it accommodates for the cases where there is no energy deposition in the target, e.g. when the decay radiation is absorbed before it can reach the target. Together, a spectral template represents the probability that a decay of nuclide  $X$  in source volume  $V$  causes an energy deposition in the  $i$ -th energy bin. We note that the *energy bin index*  $i$  depends on the energy range  $E_j$  of the data set  $D_j$  to which the spectral template should be compared. Also, the actual number of background *templates* is higher than the number of background *components*, as the same component may contribute to the background in several of the three energy ranges  $E_j$ .

The benchmark is how well the new background model can explain the reference data given the normalisation of its 84 background components<sup>1</sup> in four categories (84 free parameters) by the new LNM compared to the old model with its 88 components (30 free parameters) and normalisation by the GFM (see Appendix A).

## 3 Likelihood Framework

In view of the problem of normalising multiple spectral templates to make their sum fit the experimental reference data, the LNM is discussed in the following.

<sup>1</sup>We note that in table 7 we list 110 components. For the reason why we did not use all of them see Appendix D.

### 3.1 Motivation for using a Likelihood Normalisation

The LNM procedure exhibits multiple advantages in comparison to the GFM:

- Due to several processing steps during the manufacturing of CRESST's setup components, the SE may be broken within any group of radionuclides that could otherwise be assumed to be in equilibrium. For example, using chemical purification for crystal scintillators can lead to broken SE [18, 19, 25]. The LNM can overcome the assumptions of full or partial SE.
- Previously, alpha peaks were fitted and, together with all corresponding beta/gamma-peaks, they were subtracted from the data until all alpha-activities were determined. Hence, correlations are only weakly considered since the determination of the alpha decay rate affects all subsequent rates, but not vice-versa. In the LNM, correlations are inherently considered and are consistently computed as a by-product of the fitting process.
- Using the GFM, peak-less spectra could previously not be included in the fit on their own a defined activity value (e.g.  $^3\text{H}$  decays). The LNM can directly extract such contamination levels by considering the effects of flat spectra on the fit in the entire energy range.
- Spectra with the same peaks or other overlapping features can often be distinguished due to their distinct shapes in their continuous part. See fig. 2 for the case of the same contaminant  $^{40}\text{K}$  in different parts of the TUM40 detector module, causing templates with the same photopeak but different continuous parts of the spectra.

In reconsidering the fitting method of spectral templates, we address and remedy many issues of the GFM by using a powerful, self-consistent, user-friendly, and less time consuming procedure based on Bayesian statistics and the likelihood framework.

It should be noted that this is not the first direct detection DM experiment that uses a likelihood-based method to fit simulated spectral templates as part of their background model. However, this work's fit operates with 84 free floating template normalisation values on a considerably bigger parameter space than previous applications e.g. by DAMIC [26] (49 free parameters) and COSINE-100 [27] ( $\lesssim 40$  free parameters).

### 3.2 Expectation Value

The *expectation value*<sup>2</sup>  $\nu$  of the complete observable background in the  $i$ -th energy bin of the  $j$ -th energy range from all contaminants  $X$  in all source volumes  $V$  is:

$$\nu_{ij}(E_i) = \sum_V \sum_X \varepsilon_{\text{SSP},j}(E_i) \cdot \varepsilon_{g,VX} \cdot f_{VXi}(E_i) \cdot T \cdot A_{VX} \cdot m_V.$$

<sup>2</sup>Labeled  $N_{\text{obs}}$  in [13, 28].

Here,  $A_{VX}$  is the *specific source activity* of contaminant  $X$  in volume  $V$  of mass  $m_V$ .

For the sake of simplicity, hereafter we combine the contaminant index  $X$  and volume index  $V$  to the *process index*  $k$  that denotes any process that contributes to the background regardless by which contaminant or from which volume. In this sense, it can e.g. also refer to a group of nuclides in SE, which we call *SE groups* hereafter.

Rewriting eq. (2), we get [29]

$$\nu_{ij}(\boldsymbol{\vartheta}) = \sum_{k=1}^{n_p} \varepsilon_{ijk} \cdot f_{ik} \cdot \vartheta_k, \quad (3)$$

where the process index  $k$  runs up to  $n_p = 84$  and the data set index  $j$  covers the three reference data sets. Here,  $\vartheta_k = T \cdot A_k \cdot m$  is the *normalisation of the process*, i.e. the total number of decays in the source volume of process  $k$ . The *efficiency of the spectral template*  $\varepsilon_{ijk} = \varepsilon_{\text{SSP},j}(E_i) \cdot \varepsilon_{g,k}$  is the ratio of observable events over total decay events. The vector of parameters to be marginalised  $\boldsymbol{\vartheta}$  consists of the normalisation values  $\vartheta_k$ . Note that the empiric PDF  $f_{ik}$  is normalised to the number of simulated events which reach the detector crystal and deposit any energy.

The uncertainty of eq. (3) can be calculated using standard error propagation [30] as was done in [31].

### 3.3 Likelihood Model

The  $i$ -th energy bin in data set  $D_j$  contains a certain *number of measured events*  $n_{ij}$  with Poissonian fluctuations that are independent of all other bins. Using the expected number of detected events  $\nu_{ij}$  and the measured number of events  $n_{ij}$ , one can utilise the Poissonian PDF,

$$P(n_{ij}; \nu_{ij}) = \frac{\nu_{ij}^{n_{ij}} e^{-\nu_{ij}}}{n_{ij}!}, \quad (4)$$

to construct the extended binned likelihood<sup>3</sup> function [29, 32],

$$\mathcal{L}_j(\boldsymbol{\vartheta}) = \prod_{i=1}^{n_{\text{bin}}} \frac{\nu_{ij}^{n_{ij}} e^{-\nu_{ij}}}{n_{ij}!}. \quad (5)$$

For numerical stability we use in the following the extended binned *log-likelihood* function,

$$\log \mathcal{L}_j(\boldsymbol{\vartheta}) = \sum_{i=1}^{n_{\text{bin}}} (n_{ij} \log \nu_{ij} - \nu_{ij} - \log n_{ij}!). \quad (6)$$

The last step in constructing the full likelihood function used in knowledge updating is to combine the likelihoods of

<sup>3</sup>We note that often in literature, the *negative log-likelihood* is used, allowing the use of popular minimisation tools.

the different energy regions  $E$ : low, medium, and high energy reference data (see section 2). The three data sets  $D_l$ ,  $D_m$ , and  $D_h$  can be interpreted as a single data set, making their respective log-likelihoods additive,

$$\log \mathcal{L}_{\text{comb}}(\boldsymbol{\theta}) = \log \mathcal{L}_l + \log \mathcal{L}_m + \log \mathcal{L}_h, \quad (7)$$

which is the combined extended binned log-likelihood.

### 3.4 Priors and Nuisance Parameters for Bayesian Inference

Equation (7) is then used as goodness-of-fit (GOF) measure in Bayesian inference of the parameters  $\boldsymbol{\theta}$ . For this, we use an adapted version of the multi-template fitter from the Bayesian Analysis Toolkit (BAT) [33]. We use the default settings, i.e. the Metropolis-Hastings algorithm (MHA), to efficiently marginalise the posterior parameter distributions. The convergence of the fitting process is discussed in section 5.

Unrestricted flat priors were used for parameters where no previous estimate exists. If activity measurements exist, the priors are Gaussian. In case an upper limit was determined, the prior is a uniform distribution with an upper boundary. Measured limits of the NER components applied in this work can be found in table 1. Additionally, we use the outcome of the previous background model [13] as priors for this model.<sup>4</sup>

In this work, no marginalised parameter is a nuisance parameter, as we are interested in the activity values of each nuclide.

### 3.5 Implementation and Fit Quality

One marginalisation technique that is widely used today [34] is the generalisation by Hastings [35] of the Metropolis algorithm [36]. It utilises Monte Carlo *Markov chains* (MCMC), which are a sequence of correlated samples such that a random element  $X_{n+1}$  depends only on the previous element  $X_n$ . For each point, a new proposal  $X_{n+1}$  is generated according to a *candidate-generating function*, also referred to as *proposal function*. The chain visits regions with high posterior densities more often but is still able to break free to explore new regions with a potentially higher posterior mode. For a more detailed overview of the MHA, we refer to [37, 38].

The MHA, as implemented in BAT, is split in two separate phases: the *prerun phase* and the *main run phase*. During the prerun phase, the scale parameters of the MCMC's proposal function are adjusted. This ensures that the high-dimensional posterior density can be efficiently marginalised. In the main run phase, the scaling parameters of the proposal function are fixed and the MCMC explores the posterior density.

<sup>4</sup>The influence on the final fit result was studied and found to be negligible while speeding up the convergence.

Note that the MHA is *not* optimised to find a posterior mode but rather to sample the distribution. An optimised algorithm for mode finding is e.g. the simulated annealing algorithm (SAA) [39]. It works very similarly to the MHA with the difference that the acceptance probability is regulated to encourage motion towards the global mode. While the SAA also creates samples of the distribution, it cannot be used for sampling like the MHA since it is strictly not an MCMC technique. Hence, in this work the MHA is used for the sampling of marginalised distributions while SAA followed by MINUIT [40] is used for global mode finding.

In practice, not a single but multiple MCMCs run in parallel to ensure that the global mode is sampled. The chains are initialised at different positions in the parameter space and should converge after a certain number of steps. Otherwise, they are identical to each other. In this work's fit, eight chains were used corresponding to a *high* precision setting of BAT. Using eight chains is a compromise between precision and computational resources.

In order to monitor the convergence of the fit, we check whether the chains are mixed, i.e. explore the same parameter space. This can be done with the  $r$ -value [41]. It compares the mean and variance of the expectation value of  $\vartheta_k$  for a single chain with the corresponding quantities of multiple chains. For mixed chains, the ratio of these values approaches unity. A commonly used convergence criterion [29] has been set as  $r < 1.1$  also for this work.

Having assured convergence of the fit, we use multiple well-known statistical similarity measures that quantify the GOF to the experimental data, see [31]. Additionally, we use two measures that especially helped us by quantifying improvements of the model in an intuitive manner. Firstly, the *reproduction percentage* or *coverage* is defined as the ratio of expected events, as yielded by the normalisation of templates, over the measured number of events in a data set  $D_j$ ,

$$\zeta_j = \frac{N_{\text{MC}}}{N_{\text{exp}} \Big|_j} = \frac{\sum_{i=1}^{n_{\text{bin}}} \nu_{ij}}{\sum_{i=1}^{n_{\text{bin}}} n_{ij}}. \quad (8)$$

It is the main statistical similarity measure between simulated and experimental data in [13, 28]. Note, however, that eq. (8) does not consider the spectral shape.

To mitigate this issue and provide a similarly intuitive statistical similarity measure that takes the shape into account, J. Burkhart developed the *explainable percentage (EP)* [31]. It reflects the percentage of events which are well-described by the overall fit and is defined as

$$EP_j = \frac{\sum_{i=1}^{n_{\text{bin}}} \Theta(p_c(n_i; \nu_i) - \alpha) \cdot n_i}{\sum_{i=1}^{n_{\text{bin}}} n_i}, \quad (9)$$

where  $\Theta(x)$  is the Heaviside step function, and  $p_c(n_i; \nu_i)$  is the central  $p$ -value [42, 43] in the  $i$ -th bin, which is the most-commonly used  $p$ -value when constructing two-sided

hypothesis tests. We assume a *nominal statistical significance* of  $\alpha = 0.01$ , which corresponds to  $\sim 2.58\sigma$ . The Heaviside step function acts as a hypothesis test with the null hypothesis being that the *true* value of the expected number of detected events,  $\nu_i^t$ , is indeed given by the predicted value  $\nu_i$  from the model, so  $\nu_i^t = \nu_i$ . If the null hypothesis is rejected, i.e. if the central  $p$ -value is less than the nominal significance level  $\alpha$ , we take the events in bin  $i$  to be *not explainable* by the model. For more details of this similarity measure, refer to [31].

As another useful application of the *EP*, we will present the *hypothesis plot* [31] as fig. 4. That is, we plot the fit and reference data together with a colour-coded background that summarises the results of the several hypothesis tests that are being conducted in each energy bin  $i$  during the evaluation of eq. (9). The colour-coding is mainly a visual tool to identify energy ranges where the fit significantly diverges from the data. The colour-values are Weierstrass-smoothened, i.e. convolved with a Gaussian, to highlight energy ranges rather than single bins. In comparison to a conventional residual plot, the hypothesis plot contains information about the GOF that is easier to interpret.

#### 4 Contamination Levels as Prior for Likelihood Normalisation

For the IR, IC, and AER background components, we use contamination levels obtained in our previous work [13] via GFM from the reference data as priors for the likelihood normalisation. This is due to the absence of activity values or limits from dedicated screening measurements. For the contaminants that cause the NER, we previously used activity limits for the heads of natural decay chains for copper from the CUORE experiment [44], which we assumed to be from the same batch. For this work, we use limits for the same radionuclides and  $^{40}\text{K}$  (in addition) obtained from our own measurements during a screening campaign, which was initiated to define the level of radiopurity in different materials used and planned to be used by the CRESST experiment.

The NER background component originates from a copper housing produced from electrolytic tough pitch type copper, also known as NOSV, which has 99.9975% purity and is suitable for cryogenic use. NOSV copper is extensively used in the experiment for the construction of detector modules, the detectors' holding structure, and components of the cryogenic infrastructure.

To determine the radiopurity of a copper sample, we used inductively coupled plasma-mass spectrometry (ICP-MS) and gamma-ray spectrometry using a high-purity germanium (HPGe) detector. The samples' preparation procedure for both methods, including commonly known surface cleaning treatments, is described in Appendix C.1. A short description of the measurement using an HPGe detector is presented in Appendix C.2. The details of the ICP-MS measurement

Table 1: Specific activities of different contaminants measured in NOSV copper samples from CRESST in comparison with limits from CUORE [44] used with *Gaussian Fit Method* for the previous work. Limits for high purity germanium detection are at 68% C.L. and for inductively coupled plasma-mass spectroscopy detection, they are at 95% C.L.

Component	Specific activity / $\mu\text{Bq kg}^{-1}$		
	HPGe	ICP-MS	CUORE values [44]
$^{238}\text{U}$	-	< 6.2	< 65
$^{238}\text{U}/^{234}\text{Th}$	< 3500	-	-
$^{238}\text{U}/^{234\text{m}}\text{Pa}$	< 760	-	-
$^{238}\text{U}/^{226}\text{Ra}$	< 20	-	-
$^{235}\text{U}$	< 50	-	-
$^{232}\text{Th}$	-	< 2	< 2
$^{232}\text{Th}/^{228}\text{Ra}$	< 24	-	-
$^{232}\text{Th}/^{228}\text{Th}$	< 20	-	-
$^{137}\text{Cs}$	< 5.6	-	-
$^{40}\text{K}$	< 190	-	-
$^{60}\text{Co}$	$46 \pm 6$	-	-
$^{59}\text{Fe}$	$42 \pm 11$	-	-
$^{58}\text{Co}$	$500 \pm 50$	-	-
$^{57}\text{Co}$	< 140	-	-
$^{56}\text{Co}$	$54 \pm 8$	-	-
$^{54}\text{Mn}$	$51 \pm 9$	-	-
$^{48}\text{V}$	< 40	-	-
$^{46}\text{Sc}$	$29 \pm 6$	-	-

are given in Appendix C.3. The results of both are listed in table 1. The values obtained for radionuclides from cosmogenic activation ( $^{46}\text{Sc}$  to  $^{60}\text{Co}$ ) and for  $^{137}\text{Cs}$  are planned to be included in a future extended background model.

In summary, the limit of  $^{238}\text{U}$  achieved in this work is more sensitive compared to the one from CUORE [44], which shows that in the previous work [13] the contribution of NER was overestimated.

#### 5 Outcome of the Fit Process

Using the activity values from [13] as priors for the IR, IC, and AER components, and the lowest limit for each nuclide from table 1 for the NER component, we executed the Bayesian likelihood normalisation on the Vienna computing cluster CLIP. A typical, parallelised run takes less than 24 CPU hours.

Figure 5 shows the convergence of all eight MCMCs during 18 000 prerun iterations (see section 3.5). Using multiple Markov chains ensures a more robust marginalisation and reduces the risk of getting stuck in a local mode.

All 84 parameters are marginalised in parallel; as an example, fig. 6 shows the evolution of the expected activity

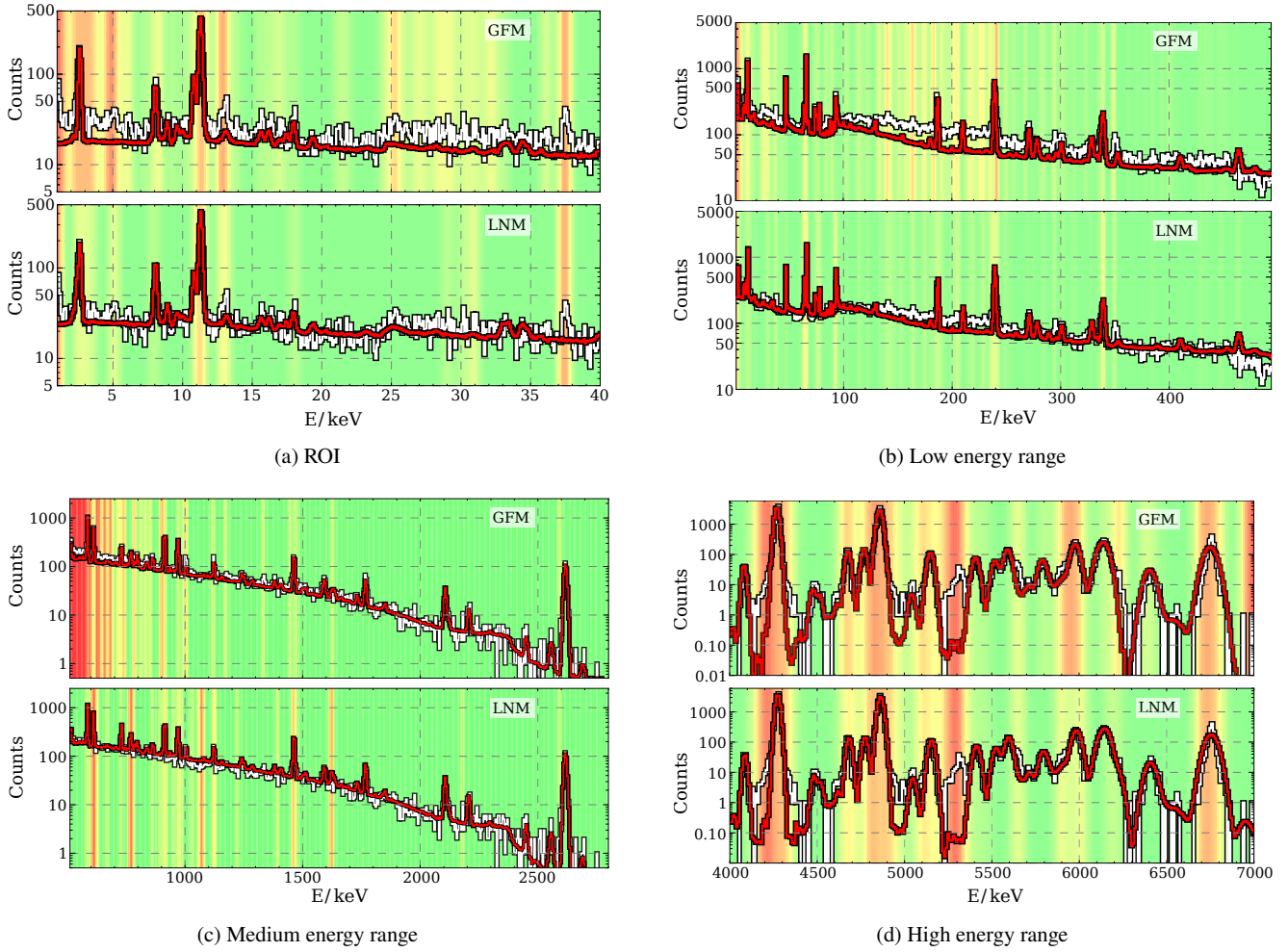


Fig. 4: Hypothesis plots comparing the performance of the updated *Gaussian fit method* (GFM, see [Appendix A](#)) in the respective *top* panel to the newly developed *likelihood normalisation method* (LNM) in the respective *bottom* panel for (a) the ROI with 100 eV binning, (b) the low energy range with 1 keV binning, (c) the medium energy range with 5 keV binning, and (d) the high energy range with 10 keV binning. The *white line* represents the experimental data, the *red line* represents the fit result. The background colour shows the result of hypothesis tests (see eq. (9)) with Weierstrass-smoothened colour values. Each bin is coloured according to the acceptance (*green*) or rejection (*red*) of the null hypothesis that fit and data agree.

value  $A_{234\text{Th}}$  of  $\text{IR } ^{234}\text{Th}$  decays. After 18 000 iterations in the prerun, the chains appear to be mixed, considering the agreement between all chains within each parameter.

This conclusion is further supported by the fact that the  $r$ -values of all 84 parameters, which represent the activities of 84 decay processes, fall below the limit of 1.1 within the adjustment phase, see fig. 5.

The main run phase now marginalises the posterior distribution for 2 500 iterations to determine the parameters' mean values, uncertainties, and correlations. Figure 7 depicts an exemplary marginalised distribution together with its prior. As can be seen there, the marginalised posterior distribution of the IR parameter  $A_{234\text{Th}}$  agrees well with the value found in [13], i.e. the prior. However, the uncertainty is considerably smaller as can also be seen in table 7.

## 6 Discussion of Fit Results

Overall, this LNM-based work can attribute significantly more background than the work based on GFM: measured as explainable percentage  $EP$  (eq. (9)), the increase in the ROI goes from 64.5 % for the GFM to 82.7 % for the LNM, see table 3. Measured as coverage  $\zeta$  (eq. (8)), this is an improvement in the ROI from 74.6 % to 93.9 %, see table 2.

This improvement is also supported by e.g. the Kolmogorov-Smirnov (KS) divergence as GOF: it drops from 0.029 for the GFM to 0.024 for the LNM in the ROI. This means that a two-sample KS test, i.e. whether the combined fit spectrum and the experimental background data have the same underlying PDF, can be rejected at significance levels down to  $10^{-7}$  ( $5.2\sigma$ ) for the GFM but only down to  $3 \cdot 10^{-5}$



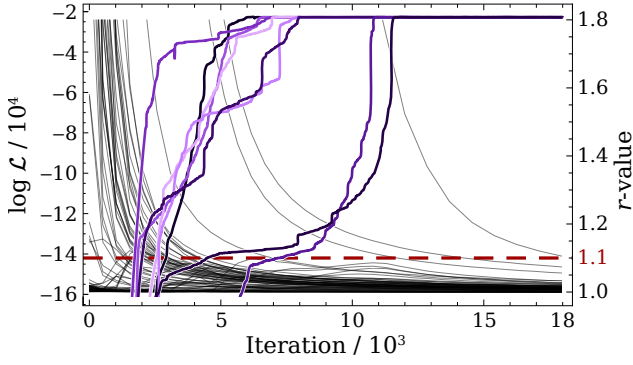


Fig. 5: Log-likelihood during the prerun phase for all eight Monte Carlo Markov chains (*purple solid lines*; *left y-axis*). The chains are identical but start at different positions in the parameter space to make the fitting procedure more robust against getting stuck in local modes. The  $r$ -value of all 84 parameters are shown as *black lines*, the convergence threshold value of 1.1 is drawn as *dashed, red line* (*right y-axis*).

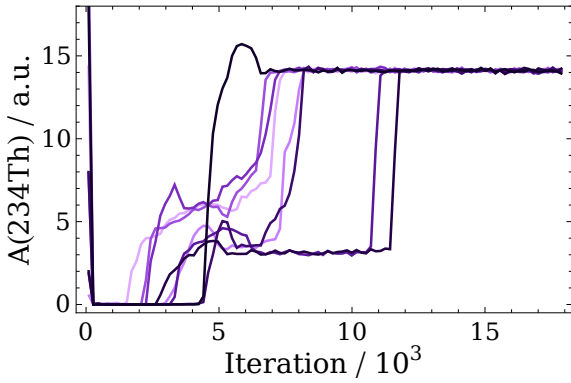


Fig. 6: The evolutions of the IR  $^{234}\text{Th}$  activity value in arbitrary units, during the prerun phase for all eight Monte Carlo Markov chains (*purple lines*). The chains are identical but start at different positions in the parameter space to make the fitting procedure more robust against getting stuck in local modes.

( $4.0\sigma$ ) for the LNM: even though in both cases the evidence for a different underlying probability distribution is high (i.e. the fitted spectrum misses some observed background components), the test rejects the LNM less strongly (i.e. the LNM can fit the background better). To avoid systematic biases, we evaluate also other GOF metrics, see [31] for the results; all of them confirm this improvement.

In the following, we will present the outcome of the LNM with respect to the GFM in terms of: the contribution of individual contaminants from the four background categories IR, IC, NER, and AER, to the combined background spectrum; the power of the LNM to handle correlated contaminants;

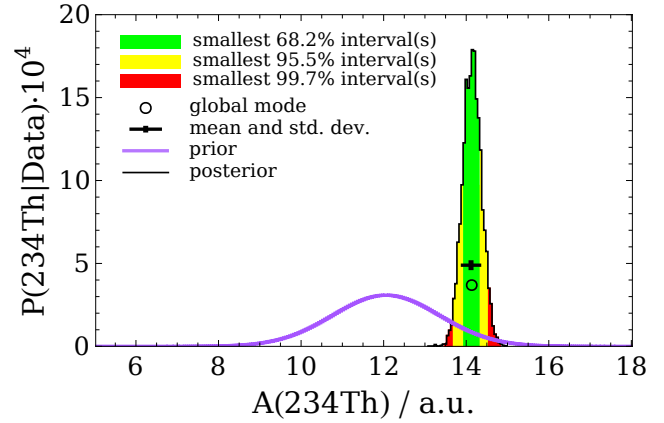


Fig. 7: The 1D marginalisation of the activity of IR  $^{234}\text{Th}$  (*coloured histogram*) in arbitrary units, together with its prior (*purple histogram*).

the improved overall spectral agreement; and the impact of omitting the SE assumption on the results.

For the convenience of the reader we first introduce the relevant figures and tables to which we will frequently refer:

- The activity values  $A$  of each background component as obtained with both methods are listed in table 7.
- Figures 9 to 12 show the related LNM background components in comparison to the reference data in the respective energy range.
- The coverage  $\zeta$  (eq. (8)) for each energy range is listed in table 2 and its decomposition into the four background categories is given in table 4 and shown in fig. 13 in comparison with GFM results.
- The statistical agreement with the experimental reference data in terms of explainable percentages  $EP$  (eq. (9)) is listed in table 3 and shown in the hypothesis plots fig. 4 (see also section 3.5).

## 6.1 Alpha Background

The spectrum in the high energy range consists mostly of clearly visible peaks of alpha-decaying nuclides. Due to their short interaction lengths, these alphas stay inside the crystal and belong completely to the IR background. The feature-rich data are well usable for both GFM and LNM, hence the coverage improved only by 2.0% (table 2) to 100.2%<sup>5</sup>. Compared to the GFM, the LNM is able to improve the spectral agreement by 7.2% (table 3) in terms of  $EP$ .

<sup>5</sup>This overestimation is of no concern, as it is only *local* to the high energy data set; the *global* coverage of all three data sets with 99.6% does not overestimate the background.

With our current study, we find the greatest improvement in the reconstruction of the  $^{234}\text{U}$  peak at 4.858 MeV <sup>6</sup> (fig. 4d). Furthermore, we significantly improve the agreement between simulation and data in the energy range between the  $^{227}\text{Th}$  peak at 6.147 MeV and the  $^{220}\text{Rn}$  peak at 6.405 MeV (fig. 13d): here the LNM can attribute the tail to the right of  $^{227}\text{Th}$  to *individual decays* of  $^{212}\text{Bi}$ , increasing the activity nearly two-fold, see table 7, compared to the value assigned in the GFM based on SE assumptions. As the daughter nuclide  $^{212}\text{Po}$  only has a half-life of 294 ns, a substantial amount of  $^{212}\text{Bi}$  decays should be removed from the reference data as  $^{212}\text{Bi} \rightarrow ^{212}\text{Po}$  pile-up events, hence the obtained  $A_{212\text{Bi}}$  value can be only a lower limit. Since this would further heighten the excess over the SE-value, its plausibility is currently under investigation.

Similarly, the LNM can attribute the few events to the right of the  $^{211}\text{Bi}$  peak at 6.750 MeV to *individual decays* of  $^{219}\text{Rn}$ , whereas the GFM can only calculate the *total*  $^{219}\text{Rn}$  activity, i.e. including pile-up events  $^{219}\text{Rn} \rightarrow ^{215}\text{Po}$  ( $T_{1/2,215\text{Po}} = 1.781$  ms), from SE assumptions. Consequently, the value for  $A_{219\text{Rn}}$  found by LNM is well below the SE-values assumed in the GFM.

As the used background model considers only bulk contaminations, neither the GFM nor the LNM can reproduce the peak at 5.304 MeV that is caused by  $^{210}\text{Po}$  contamination on the surface of the target crystal (see [23] for details). Currently, we extend our background model to include surface contaminations, also to study the possibility that the tails around the  $^{238}\text{U}$  peak (4.270 MeV), and between the  $^{234}\text{U}$  (4.857 MeV) and  $^{231}\text{Pa}$  (5.159 MeV) peaks (see fig. 12) may be caused by partial energy collection close to surface.

## 6.2 Radiogenic Beta and Gamma Background

Besides the dominant alpha lines, the background in the high energy range also has a contribution of beta/gamma decays of  $^{208}\text{Tl}$ : due to the slow detector response of  $\mathcal{O}(\text{ms})$ , beta decays of IR  $^{208}\text{Tl}$  and subsequent gamma transitions to the ground state of  $^{208}\text{Pb}$  cannot be resolved but are reconstructed as one event with a combined energy deposition up to  $\sim 4.9$  MeV (cf. fig. 12). Whereas the GFM had to reconstruct the high energy range solely from alpha decaying contaminants, the LNM can also consider the featureless, high-energy tail of the  $^{208}\text{Tl}$  template.

Up to an end-point of 3.269 MeV, the beta spectrum of individual  $^{214}\text{Bi}$  decays are a prominent contribution (cf. fig. 11). Again, the GFM values are higher than the LNM ones (table 7), as the former includes the pile-up events  $^{214}\text{Bi} \rightarrow ^{214}\text{Po}$  ( $T_{1/2,214\text{Po}} = 163$   $\mu\text{s}$ ).

<sup>6</sup>The literature data for energy levels, half-lives  $T_{1/2}$ , and branching ratios  $BR$  are taken from the IAEA Live Chart of Nuclides: <https://www-nds.iaea.org/relnsd/vcharthtml/VChartHTML.html>

Beta/gamma-decaying nuclides are the dominant source for background below the prominent photopeak of  $^{208}\text{Tl}$  at 2.615 MeV. As shown in figs. 9 to 11, each beta/gamma template has an individual end point and hence a different slope. This information is not usable with the GFM but give the LNM a sensitivity also to rather smooth, peak-less templates. Together with the improved background model (see Appendix B), which was enabled by the LNM, this allows for a better reproduction of flat background parts in the 1 keV–8 keV, the 25 keV–40 keV, and the 100 keV–300 keV (cf. figs. 13a to 13c).

Below 140 keV, the background is dominated by IR components (cf. fig. 13b); in the ROI it reaches a coverage of 48.4 %, see table 4, with  $^{234}\text{Th}$  being the most prominent contaminant. The NER background, caused by the detector holder made of NOSV copper, stays the least important background category within the ROI, but increased to 1.5 %. This is mainly driven by higher activities for  $^{210}\text{Pb}$ : with a  $Q$ -value of 63.5 keV, it contributes to the ROI and low energy range (figs. 4b and 9). Preliminary results of ongoing screening measurements indicate a  $^{210}\text{Pb}$  activity of  $\mathcal{O}(\text{mBq kg}^{-1})$ , which is much higher than the fitted value of  $A_{210\text{Pb,NER}} = (61 \pm 3) \mu\text{Bq kg}^{-1}$ . We found that the simplified geometry we applied in our current background model most likely causes a strong overestimation of the geometric efficiency  $\varepsilon_g$  (see eq. (1)) for NER  $^{210}\text{Pb}$ : an unrealistically low activity seems adequate to explain the observed background rate. Hence, the value stated in table 7 should be regarded as a lower limit. To mitigate this issue, a simulation with a more detailed geometry is currently in preparation and will be used in a future extended background model. We want to point out that because of the more precise screening information used in combination with the LNM (see table 1), nearly all other contaminants in the NER category, with the exception of five nuclides (see table 7), have activities that are either below  $< 0.01 \mu\text{Bq kg}^{-1}$  or compatible with zero within  $2\sigma$ . This leads to a decreased importance of NER background components in the medium energy range (fig. 13c).

Due to the stricter limits on NER contaminants we used for the LNM, the remaining gamma peaks in the medium energy range (figs. 11 and 13c), which can be neither attributed to IR nor to NER, are now exclusively attributed to AER, resulting in an increased overall contribution of AER and making it the second most prominent background category in the ROI with an increased coverage of 23.5 % (table 4).

## 6.3 Cosmogenic Background

The IC background is present only in the low energy range and the contribution of it with its three constituents  $^3\text{H}$ ,  $^{179}\text{Ta}$ , and  $^{181}\text{W}$ , increased from 17.6 % to 20.5 % in the ROI (table 4). Within  $2\sigma$  around the respective mean values the individual activities stay the same between the GFM and the LNM with

one exception (table 7). This is to be expected, as the sharp peaks associated with these contaminants make them equally suitable for both the GFM and the LNM. For the electron capture (EC) decay of  $^{179}\text{Ta}$  the LNM, contrary to the GFM, is able to disentangle the three overlapping peaks due to EC from the  $M_1$ ,  $M_2$ , and  $M_3$  shells.

The exception is  $^3\text{H}$ , whose completely peak-less, pure beta spectrum with an end point at 18.591 keV cannot be processed at all by the GFM due to its definition, i.e. relying on peaks. Hence, GFM-based background studies ([13, 28], Appendix A) estimated the  $^3\text{H}$  activity  $A_{3\text{H}}$  from ACTIVIA calculations to  $(24.2 \pm 0.9) \mu\text{Bq kg}^{-1}$ . In contrast, LNM-based studies, like this work, can naturally consider such peak-less spectra. To compensate for missing background at low energies, the LNM-based fit increased  $A_{3\text{H}}$  by almost a factor of three to  $(64 \pm 4) \mu\text{Bq kg}^{-1}$ , making up more than 10 % of the flat background in the 1 keV–20 keV range. Given that CRESST searches for light DM and thus a precise description of our background at low energies is crucial, the study of the  $^3\text{H}$  contamination is of high interest. Clearly,  $A_{3\text{H}}$  relies on the assumptions of the applied background model, especially on unknown contaminants at low energy, and hence may change in any future update of our model. From extended ACTIVIA calculations [45], we know already that we can expect further cosmogenically activated radioisotopes in our crystals, which will be introduced in a future extended background model.

#### 6.4 Correlations between Similar Contaminants

The sensitivity of the LNM to continuous parts of the spectral templates can allow it to disentangle background components caused by the same contaminant but originating from different volumes. Of course, the ability to do so depends on how much the continuous parts differ in shape and slope.

Figure 2 compares the template shapes from different geometric sources on the example of  $^{40}\text{K}$ . Hence, we allowed independent  $^{40}\text{K}$  contaminations in the NER, AER, and IR background categories. In contrast, the GFM left no other choice but to attribute all  $^{40}\text{K}$  contributions to one of the three background categories for which we arbitrarily chose AER.

However, also the discrimination power of the LNM is limited: even though the LNM makes a strong attribution of  $^{40}\text{K}$  solely to AER and none to NER and IR, we note the strong anti-correlation between the AER and the NER component, see fig. 8. This means that the continuous spectral parts of the NER and AER components are too similar to allow for an unambiguous discrimination, see the inset in fig. 2 that shows the slight differences at low energies between the NER and AER templates. A contribution from the IR component, on the other hand, can be readily excluded since no significant anti-correlation can be observed; here the spectrum is significantly different from the NER and AER templates, see fig. 2. In

general, a strong anti-correlation indicates uncertainty of the fit which template to use since the corresponding parameters tend to complement each other. Small changes in the starting conditions (like noise) might lead to large changes of the parameters.

Further strong anti-correlations are observed for  $^{210}\text{Pb}$ ,  $^{226}\text{Ra}$ , and  $^{234}\text{Th}$  when the same nuclide is placed in different volumes, and for  $^{40}\text{K}/^{234}\text{Th}$ ,  $^{218}\text{Po}/^{227}\text{Th}$ , and  $^{226}\text{Ra}/^{234}\text{U}$  when these nuclides are placed in the same volume, see fig. 8.

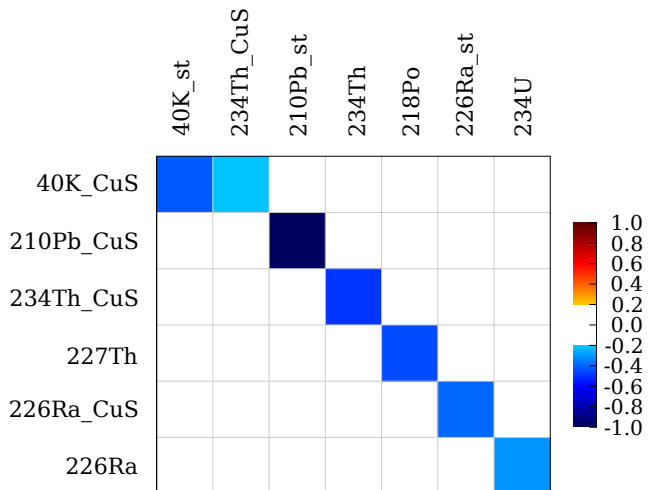


Fig. 8: Correlations between parameters  $\theta_k$  (see eq. (3)) of the likelihood normalisation method. Template names ending in “st” refer to NER components while names ending in “CuS” refer to AER components. Only the part of the correlation matrix with absolute values larger than 0.2 is shown.

#### 6.5 Overall Spectral Agreement

The spectral agreement of the LNM-based background fit to the reference data provides a better description of the background compared to the GFM. The explainable percentages (see eq. (9)) are improved in each energy range separately, for the combined range it is improved by 7.9 %. As shown in the hypothesis plot fig. 4d, we now better reproduce the  $^{223}\text{Ra}$  peak at 5.978 MeV in the high energy range. In the ROI (fig. 4a), the peaks around 2.6 keV and 11 keV caused by EC decays of  $^{179}\text{Ta}$  from the M and L shells, respectively, match better. Also the tension between model and data around 25 keV and below 5 keV is mended, the latter due to the increased  $^3\text{H}$  contribution. In the low and medium energy ranges, the LNM enables a better reproduction of the continuous parts of the observed background, resulting in less tension in the hypothesis plots between 120 keV–220 keV and 500 keV–800 keV, see figs. 4b and 4c.

There are still tensions at  $\sim 13$  keV,  $\sim 37.5$  keV, and  $\sim 41.8$  keV, where our model cannot reproduce peaks. In an attempt to explain the peak at  $\sim 13$  keV, we added  $^{228}\text{Ra}$ , which features a gamma line at 13.52 keV, to the AER component of our model, allowing essentially an unconstrained contribution of  $^{228}\text{Ra}$ . However, the LNM-based fit set  $A_{228\text{Ra,AER}} < 0.01 \mu\text{Bq kg}^{-1}$  (table 7) and therefore excludes it as a source for the observed peak. These missing peaks and the remaining difference of the flat background between 140 keV–240 keV (figs. 4b and 10) suggests that there might be additional background sources that were not considered so far, e.g. contaminants in the scintillating and reflecting polymeric foil that is placed in the detector modules. Work is going on to extend our future background model addressing this issue.

## 6.6 Secular Equilibrium Assumption

Leaving the 84 components of the LNM unconstrained by SE assumptions raises the question about the physical plausibility of the obtained results. Due to the time elapsed between modifying the radiochemical composition of the crystals during production and the start of data taking, one can assume that at least some sub-groups of the natural decay chains retain secular equilibrium. However, the purpose of this work is to demonstrate the technical capabilities of the LNM and its potential to cross-check SE assumptions with respect to the GFM since assuming no SE allows the LNM to compensate for unidentified or unused background components. In addition, as we showed in [21], even without imposing partial SE a priori, LNM recovers most of the partial SE a posteriori. Based on the results from [21], we currently study the impact of different strictness levels of SE constraints on the results of the LNM approach.

Table 2: Comparison of coverages (see eq. (8)) between the normalisation using the Gaussian fit method (*GFM*) (Appendix A) and this work’s likelihood normalisation method (*LNM*) in the different energy ranges (see section 2). The improvement (*Impr.*) measures the change towards 100 %:  $|\zeta_{j,\text{GFM}} - 100\%| - |\zeta_{j,\text{LNM}} - 100\%|$ .

	ROI	Low	Medium	High	Combined
GFM	74.6 %	74.6 %	88.7 %	97.8 %	84.0 %
LNM	93.9 %	94.6 %	110.4 %	100.2 %	99.6 %
Impr.	19.3 %	20.0 %	0.9 %	2.0 %	15.6 %

In conclusion, while having completely free-floating parameters might not be the physically most accurate model (it is unlikely that all SE groups are broken), it can be interesting to see the full potential of the simulated data. This can help to

Table 3: Comparison of explainable percentages (see eq. (9)) between the normalisation using the Gaussian fit method (*GFM*) (Appendix A) and this work’s likelihood normalisation method (*LNM*) in the different energy ranges (see section 2). The improvement (*Impr.*) measures the change towards 100 %:  $|\text{EP}_{j,\text{GFM}} - 100\%| - |\text{EP}_{j,\text{LNM}} - 100\%|$ .

	ROI	Low	Medium	High	Combined
GFM	64.5 %	77.2 %	88.7 %	34.4 %	68.2 %
LNM	82.7 %	88.1 %	90.9 %	41.6 %	76.1 %
Impr.	18.6 %	10.9 %	2.2 %	7.2 %	7.9 %

Table 4: Comparing the coverages of the individual background components in the energy range of interest between the normalisation using the Gaussian fit method (*GFM*) (Appendix A, table 6) as baseline and this work’s likelihood normalisation method (*LNM*). Values rounded to one decimal place.

Component	GFM	LNM
Internal radiogenic	40.7%	48.4%
Internal cosmogenic	17.6%	20.5%
Near external radiogenic	0.2%	1.5%
Additional external radiogenic	15.9%	23.5%
Sum	74.6%	93.9%

assess if an unexplained peak under partial SE assumptions is truly absent in the current simulations, or if a certain template might be able to fill the gap but is held back by SE constraints. If the latter case is true, there are two likely explanations: either SE is truly broken, or an additional source from a different component of CRESST’s setup is missing in the simulations. This can — in practice — only be determined by further simulations of a more detailed setup geometry, by considering more contaminants, and/or through dedicated screening measurements like the one carried out in this work (see section 4).

## 7 Summary and outlook

In this work we introduced the LNM to estimate the electromagnetic background of the CRESST experiment from experimental measurements on the example of the TUM40 detector module. Compared to the previously used GFM, the newly adopted LNM, based on a Bayesian likelihood fit, features three major benefits: (i) it is independent from the assumption of partial SE, (ii) it can handle peak-less background components (e.g.  $^3\text{H}$ ), and (iii) it can disentangle partially overlapping peaks (e.g. EC peaks of  $^{179}\text{Tl}$ ). Overall, it shows an enhanced capability to reproduce the observed continuous background. To improve the priors for the likelihood fit, we performed dedicated measurements of the radioactive con-

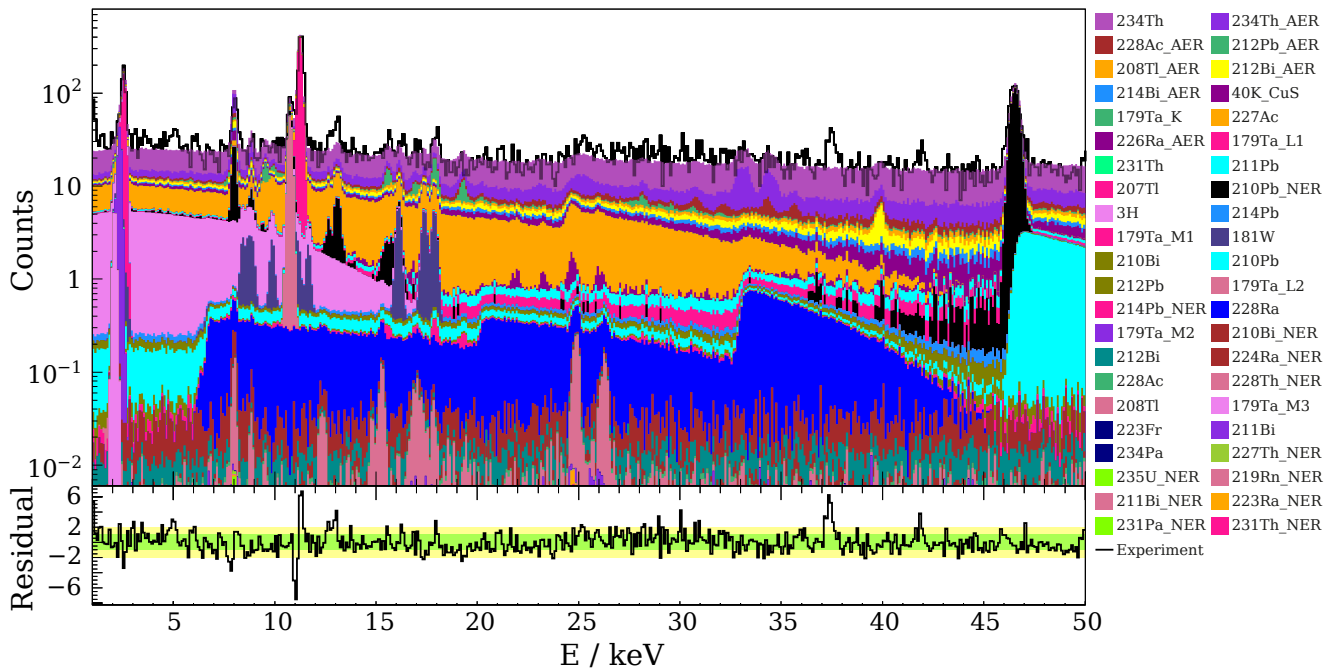


Fig. 9: Stacked plot of all templates in the ROI compared to the reference data (*black line*) with a bin width of 100 eV. The legend is ordered by the nuclides' coverages from highest (*upper left*) to lowest (*lower right*); an interactive version of this plot is provided as supplementary material.

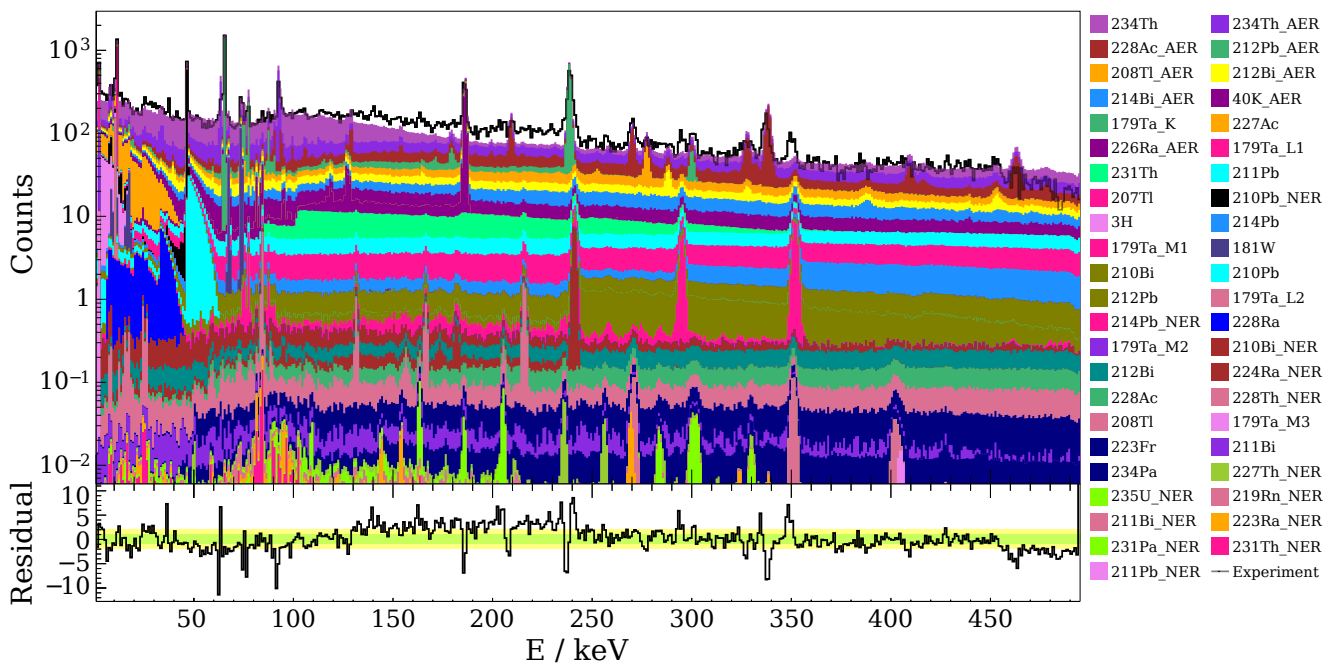


Fig. 10: Stacked plot of all templates in the low energy range compared to the reference data (*black line*) with a bin width of 1 keV. The legend is ordered by the nuclides' coverages from highest (*upper left*) to lowest (*lower right*); an interactive version of this plot is provided as supplementary material.

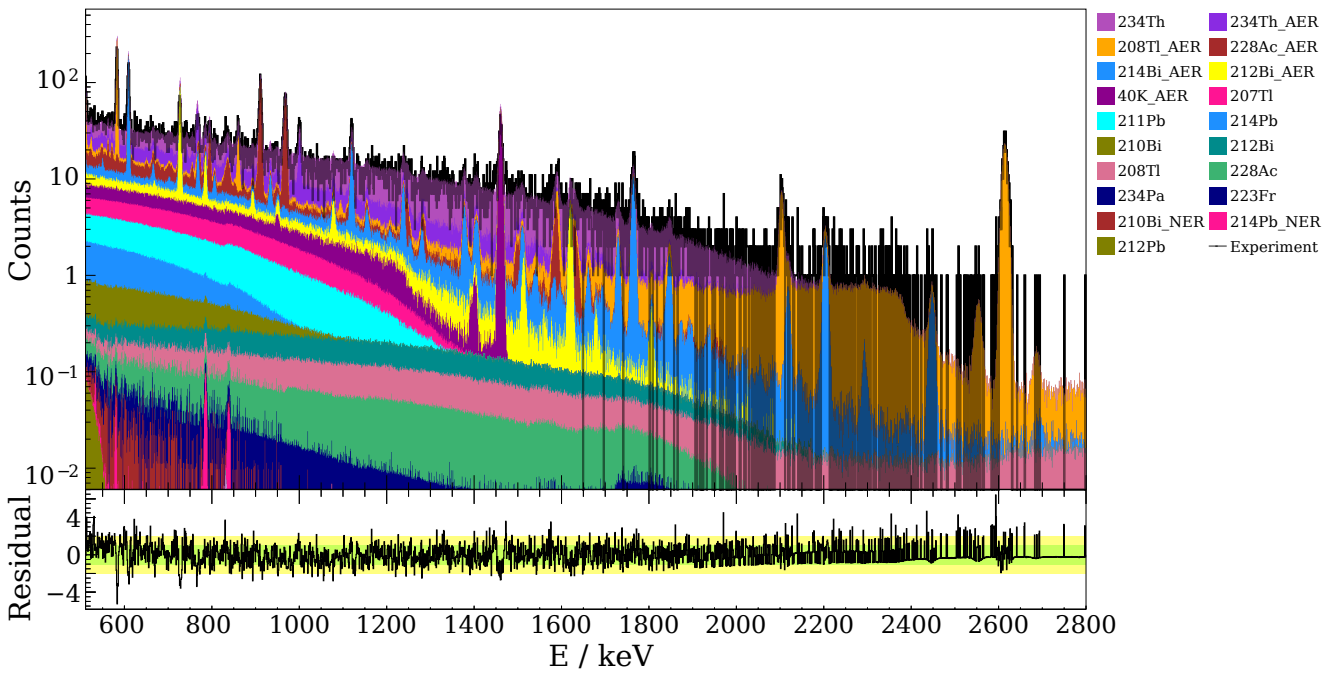


Fig. 11: Stacked plot of all templates in the medium energy range compared to the reference data (*black line*) with a bin width of 1 keV. The legend is ordered by the nuclides' coverages from highest (*upper left*) to lowest (*lower right*); an interactive version of this plot is provided as supplementary material.

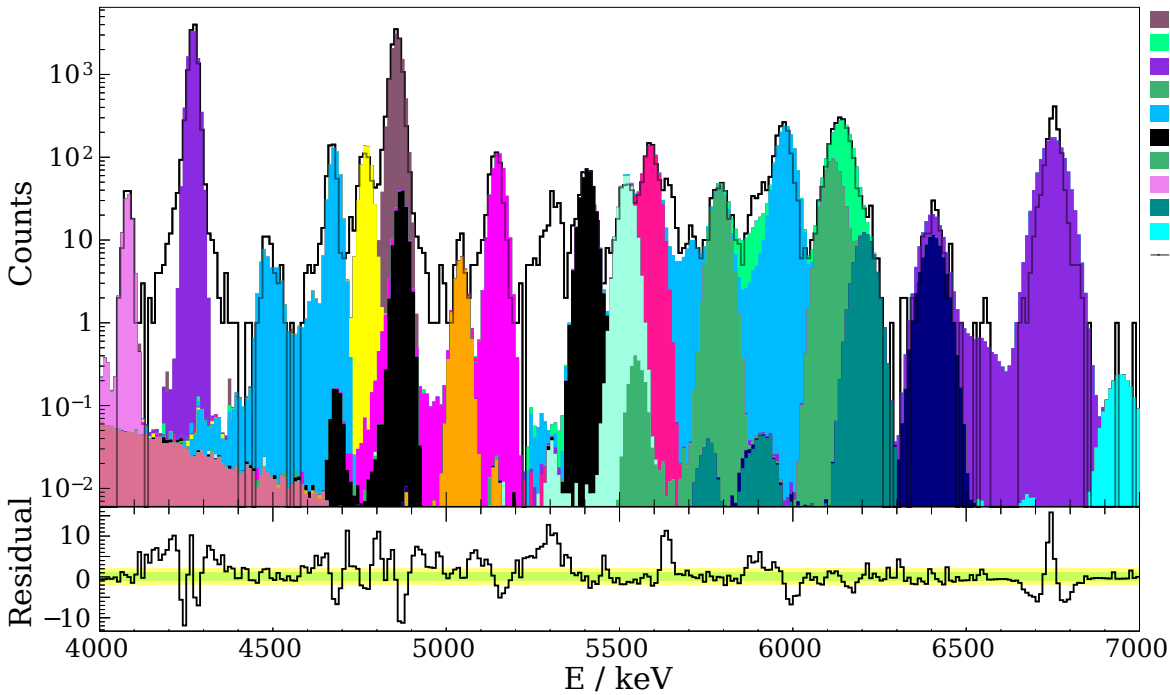


Fig. 12: Stacked plot of all templates in the high energy range with a bin width of 10 keV. The legend is ordered by the nuclides' coverages; an interactive version of this plot is provided as supplementary material. Possible sources of the events in the blank regions are currently being investigated.

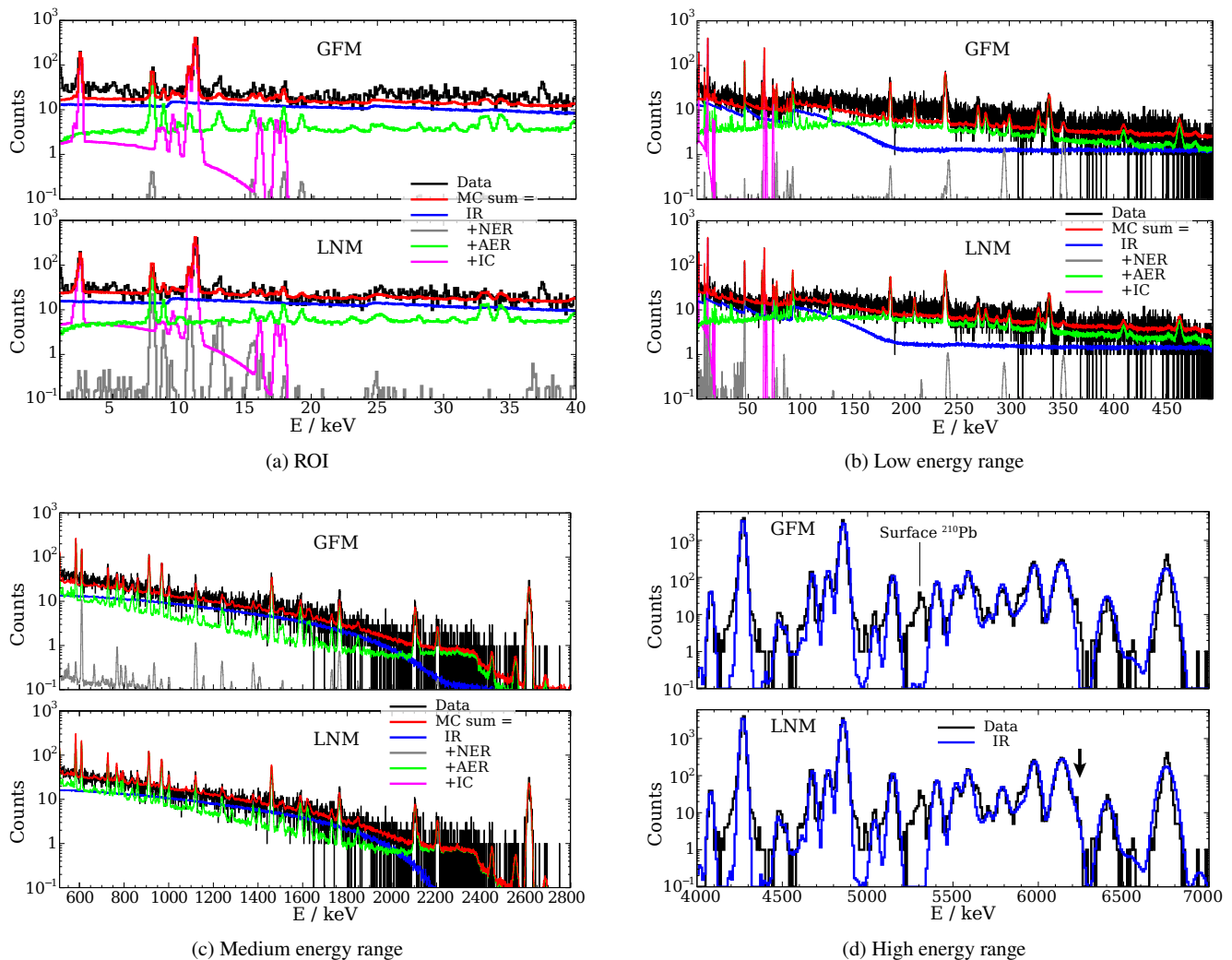


Fig. 13: Decomposition of the fitted background into *internal radiogenic* (IR, blue line), *near external radiogenic* (NER, gray line), *additional external radiogenic* (AER, green line), and *internal cosmogenic* (IC, pink line) in comparison to the experimental reference data (black histogram) for (a) the ROI with 100 eV binning, (b) the low energy range with 100 eV binning, (c) the medium energy range with 1 keV binning, and (d) the high energy range with 10 keV binning. The performance of the updated *Gaussian fit method* (GFM, see Appendix A) is shown in the respective *top* panel and the newly developed *likelihood normalisation method* (LNM) in the respective *bottom* panel. Note that the spectral shapes of the fits in (d) only appear to be identical, but feature improvements around the peaks of  $^{227}\text{Ac}$  and  $^{212}\text{Bi}$  which are indicated by *black arrows*; also the  $^{210}\text{Po}$  surface contamination is not considered in the current background model.

tamination levels in the copper used for the TUM40 detector holder in the frame of an ongoing screening campaign. The results are the most sensitive limits obtained for NOSV copper from this batch, which shows the clear overestimation of this component in the previous model.

Within the applied background model, consisting of 84 individual background components without enforced partial SE, the LNM could cover 93.9 % of the observed electromagnetic background in the TUM40 detector module in the ROI. This is a major improvement compared to the 74.6 % obtained with the previously used method. The explainable percentage

– an intuitive GOF measure introduced in this work – grew from 64.5 % to 82.7 % at a 0.01 nominal significance.

This is partially driven by a significantly higher  $^3\text{H}$  contamination in the  $\text{CaWO}_4$  crystal:  $(64 \pm 4) \mu\text{Bq kg}^{-1}$  compared to  $(24.2 \pm 0.9) \mu\text{Bq kg}^{-1}$  obtained with the GFM method. Further studies are needed to assess how robust these results are against changes of the underlying background model, e.g. by adding more background components or imposing various degrees of SE [31].

At the moment, we are actively working on improvements of our future background model. Extensive material assays

and screening campaigns are planned to provide more precise priors for the likelihood normalisation. Furthermore, we are extending our background model: we are investigating additional contaminants as potential origins of so far unidentified peaks at 13 keV, 37.5 keV, and 41.8 keV (see fig. 10) and unattributed alpha background in the 4 MeV to 7 MeV range (see fig. 12). These additional contaminants consist of dedicated surface contaminations, further cosmogenics [45], and contributions from components of the experiment not considered thus far, like the scintillating foils inside the detector modules. The approximated source geometry for the AER background is currently replaced with a detailed geometry of the cryostat. From this we expect a more precise determination of the  $^{210}\text{Pb}$  activity in external copper parts of the setup and an impact on the spectral template. We are also switching to a more recent Geant4 version. As another step, we plan to apply the likelihood normalisation method to further detector modules and different target materials, e.g.  $\text{Al}_2\text{O}_3$  and  $\text{LiAlO}_2$ .

## 8 Acknowledgments

This work has been funded by the Deutsche Forschungsgemeinschaft (DFG, German Research Foundation) under Germany's Excellence Strategy – EXC 2094 – 390783311 and through the Sonderforschungsbereich (Collaborative Research Center) SFB1258 ‘Neutrinos and Dark Matter in Astro- and Particle Physics’, by the BMBF 05A20W01 and 05A20VTA and by the Austrian science fund (FWF): I5420-N, W1252-N27. FW was supported through the Austrian research promotion agency (FFG), project ML4CPD. SG was supported through the FWF project STRONG-DM (FG1). JB and HK were funded through the FWF project P 34778-N ELOISE. The Bratislava group acknowledges a partial support provided by the Slovak Research and Development Agency (projects APVV-15-0576 and APVV-21-0377). The computational results presented were partially obtained using the CLIP cluster and the Max Planck Computing and Data Facility (MPCDF).

## Appendix A: Updated Results using the Gaussian Fitting Method

The original implementation of the GFM in [13] contains a technical shortcoming in the analysis code. It caused an underestimation of  $^{234}\text{Th}$  in the IR background component and overall an overestimation of the NER background components, especially  $^{210}\text{Pb}$ ,  $^{218}\text{At}$ ,  $^{226}\text{Ra}$ ,  $^{228}\text{Ra}$ ,  $^{228}\text{Th}$ , and  $^{234}\text{Pa}$ . Both effects nearly cancel each other out, leading to an insignificant effect on the total sum in table 6 with respect to the uncertainties.

Table 5: Activities  $A$  for individual background components over the full energy range and the resulting background rate  $R$  in the ROI according to the Gaussian fit method. Statistical uncertainties at 68 % C.L., values rounded to two significant digits on the smallest uncertainty.

Component	$A \pm \delta_{\text{stat}} \pm \delta_{\text{sys}}$ / $\mu\text{Bq kg}^{-1}$	$R \pm (\delta_{\text{stat}} + \delta_{\text{sys}})$ / $\text{kg}^{-1}\text{keV}^{-1}\text{d}^{-1}$
Internal		
Radiogenic		
$^{238}\text{U}$ decay chain	$3781 \pm 26 \pm 110$	$0.634 \pm 0.011$
$^{235}\text{U}$ decay chain	$1256.7 \pm 8.2 \pm 63.5$	$0.2326 \pm 0.0079$
$^{232}\text{Th}$ decay chain	$155.2 \pm 1.1 \pm 20.7$	$0.0184 \pm 0.0026$
Cosmogenics	$448.27 \pm 0.63 \pm 9.23$	$0.383 \pm 0.010$
External radiogenic		
Near <sup>a</sup>	$774.71 \pm 0.73$	$(5.186 \pm 0.069) \cdot 10^{-3}$
Additional	$3432.0 \pm 4.9 \pm 369.3$	$0.346 \pm 0.035$
Total sum	$9848 \pm 38 \pm 573$	$1.619 \pm 0.066$

<sup>a</sup> In this case no systematic uncertainty can be given, see [13] for details.

Table 6: Relative contribution for individual background components in the ROI according to the Gaussian fit method. Linearly combined statistical (at 68 % C.L.) and systematic uncertainties; values rounded to two significant digits on the uncertainty.

Component	Relative contribution (%)	
	Original work [13]	This work
Internal		
Radiogenic	$26.6 \pm 5.0$	$40.7 \pm 1.9$
Cosmogenic	$17.8 \pm 3.8$	$17.63 \pm 0.57$
External radiogenic		
Near	$6.3 \pm 2.1$	$0.2388 \pm 0.0028$
Additional	$17.5 \pm 4.9$	$15.9 \pm 3.2$
Total sum	$68.2 \pm 15.8$	$74.6 \pm 5.6$

To provide a reliable base to which the new likelihood normalisation presented in this work can be compared, we provide here updated results of the GFM normalisation. Updated background spectra [13, figs.11, 12] are given in fig. 13, updated contamination activities [13, table 4] and relative contributions [13, table 5] per background component, and activities per nuclide [13, tables 7 to 11] are given in tables 5 to 7, respectively.

Besides the update, we used for the spectral template the same improved energy resolution as for the LNM, see Appendix B. Beyond these, no changes to the physics and methodology outlined in [13] were applied. Especially, the NER components are still normalised to the contamination values reported by CUORE [44] and *not* to those reported in section 4 for our own copper.



## Appendix B: Improvements of the Background Model

The used background model was originally developed in [13] and further improved for this work. The changes are:

Because the original background model was the first ever developed for CRESST, the IR background component still contained radionuclides which afterwards could be omitted as it turned out that their contribution to the background is negligible, because their branching ratio is insignificant and only minimal leakage to lower energies occurs (see table 7 for details). Furthermore, in our previous work we normalised the background model solely with the GFM which lacked the capability of the LNM to discriminate between templates which share the same peaks but deviate in their continuous parts. Hence, in the previous work all activity of  $^{40}\text{K}$  had to be assigned to the AER background component and could not be given the opportunity to be shared between AER, NER, and IR.

Because the GFM cannot handle featureless, pure beta spectra, we could not directly normalise the  $^3\text{H}$  contribution to the IC background component. Instead, it was related to the activity of  $^{181}\text{W}$  via ACTIVIA [46] calculations. Furthermore, as the GFM has only limited capability to process overlapping peaks, we could not individually normalise the spectral templates of the  $^{179}\text{Ta}$  M-shells but had to treat it as one combined template. As the used Geant4 version wrongly applied the same branching ration to all shells, this was a systematic shortcoming. In total, the previous background model contained only six instead of nine IC components.

Similar as for the IR background, also the selected 28 radionuclides for the NER background category were different in the original model. As the complete observed background activity of  $^{40}\text{K}$  was originally assigned to AER, the total number of components for NER was only 28. Originally, the activities of these radionuclides were normalised to screening results from the CUORE experiment [44], which used the same batch of copper as CRESST, under the assumption of complete SE through each of the three radioactive decay chains. This was necessary because contaminations by the same radionuclide but in different volumes, here the  $\text{CaWO}_4$  target (IR background) and the detector module holder (NER background), can cause similar spectral templates which differ not in their peaks but in their continuous part. Hence, with the GFM it was not possible to normalise the NER components to the reference data in the original work, whereas in this work with the LNM it is possible.

Finally, the AER background originally consists of only nine observed nuclides:  $^{40}\text{K}$ ,  $^{208}\text{Tl}$ ,  $^{210}\text{Pb}$ ,  $^{212}\text{Pb}$ ,  $^{212}\text{Bi}$ ,  $^{214}\text{Bi}$ ,  $^{226}\text{Ra}$ ,  $^{228}\text{Ac}$ , and  $^{234}\text{Th}$ . Only after publication,  $^{228}\text{Ra}$  was identified as a possible source for a yet unidentified peak at 13 keV. As the precise origin of the AER components is still unknown, we continue to use the "Cu shell approximation" which we developed in [13].

Overall, our original background model contained 88 individual background components in four categories with 30 free parameters, compared to 84 individual components in the current work with 84 free parameters.

## Appendix C: Screening Methodology

### Appendix C.1: Copper Sample Preparation

The samples, in the form of plates, were cut from several big copper sheets kept in a storage cellar of the Weihenstephan brewery (15 m deep) close to Munich to avoid cosmogenic activation of the material.

We prepared a sample with a total mass of 95.71 kg that consists of two types of plates: 18 plates without and 16 with a hole in the centre to fill the cavity of the HPGe detector as much as possible. Their size is  $245\text{ mm} \times 245\text{ mm} \times 8\text{ mm}$  and the hole, if present, is  $\text{Ø}100\text{ mm}^2 \times 8\text{ mm}$ . In each plate, four threaded smaller holes were drilled to facilitate placing them inside the sample chamber of the HPGe spectrometer. Only one plate without hole was used for alpha spectrometry. The sample for the ICP-MS measurement was a small piece cut from one of the plates with a total mass of 34.85 g and a size of  $6\text{ mm} \times 10\text{ mm} \times 108\text{ mm}$ .

The surface oxidation caused by long time exposure to air was removed by mechanical grinding of the copper surface. Around 0.5 mm of the top layer was polished off. To further minimise the radioactive contamination of the surfaces introduced during the sample cutting and handling, the following cleaning procedure was applied:

- cleaning with acetone;
- ultrasonic bath in a mixture of alkaline cleaning solution and water;
- rinsing with high purity DI-water (resistivity value is  $18.2\text{ M}\Omega\text{ cm}^{-1}$  at  $25\text{ }^\circ\text{C}$ );
- etching in a water solution of nitric acid (70 %);
- passivation in a water solution of hydrogen peroxide (ratio 1:1) and citric acid (5 % of mass).

All used chemicals were of ultra pure quality. In fig. 14, the difference before and after cleaning of the plates is shown.

### Appendix C.2: Gamma Ray Spectrometry with HPGe Detectors

Gamma-ray spectrometry performed with germanium detectors allows to directly quantify the activity of many radionuclides contributing to the background of an experiment. The measurement was performed in the underground low background laboratory STELLA (SubTERRanean Low Level Assay) at LNGS [47, 48]. The p-type coaxial germanium detector [49–51] used for the measurement is shielded with



Fig. 14: Photos of NOSV copper samples before (*left*) and after (*right*) chemical surface cleaning.

20 cm of lead (with low level of  $^{210}\text{Pb}$ ) and 5 cm of NOSV copper. The sample chamber with a volume of  $0.0138\text{ m}^3$  is constantly flushed with boil-off nitrogen from a nearby liquid nitrogen storage tank. The total background rate of the detector between 40 and 2700 keV is  $44\text{ kg}^{-1}\text{ d}^{-1}$ . The energy resolution of the detector is 2.63 keV (FWHM) for the 1332.52 keV gamma-line of  $^{60}\text{Co}$ . The data for the copper sample were accumulated in the energy range of 50 keV–3000 keV during 2540 h.

### Appendix C.3: Inductively Coupled Plasma Mass Spectrometry

In order to remove the surface contamination due to handling and cutting, the copper sample was treated with several partial etchings by 20 mL of 4 M (Molar) solution of ultrapure nitric acid, obtained by means of a sub-boiling distillation system<sup>7</sup>. About 3 g of copper were solubilised every etching. All solutions were stored separately.

After about 70% of the copper mass was dissolved, the solution of the last etching was collected in perfluoroalkoxy (PFA) vials previously cleaned and checked. This solution was divided in two aliquots: the first was used for the measurement of the contamination in the bulk of the sample; the second was spiked with 25 pg/g of Th and U, using a reference standard solution<sup>8</sup>, to evaluate the recovery yield of the sample treatment procedure.

Subsequently, a matrix separation was carried out in columns filled with TRU resin<sup>9</sup> to pre-concentrate Th and U. Conditioning of the columns was performed by alternate rinsing steps using 4 M nitric acid and 0.1 M ammonium oxalate. Then the 4 M acid solutions containing the metal

were loaded in the columns where the analytes were eluted with 10 mL of 0.1 M ammonium oxalate.

The concentration of Th and U was measured by means of Sector Field-ICP-MS<sup>10</sup>. All the sample treatment procedures and the measurement were performed inside an ISO 6 class clean room at LNGS to reduce the risk of possible environmental contamination. The concentration of Th and U measured in the copper sample was  $< 0.5 \cdot 10^{-12}\text{ g/g}$  for both isotopes. Using conversion factors<sup>11</sup>, we receive the activities listed in table 1.

### Appendix D: Obtained Activities

Table 7 lists the activity values per background component as obtained with the updated GFM (see Appendix A) and the LNM. Some components, marked with *a*, are strongly suppressed by branching ratios  $\lesssim 0.01\%$  in their respective branch. As the previous work [13] and the updated GFM proved their insignificance for the background model, they are omitted from the LNM.

Some components, marked with *b*, undergo a pure alpha decay with a *Q*-value beyond the upper energy limit of 7 MeV of the used reference data (see section 2.2). In the previous work, the GFM assigned activities by assuming partial SE with a component within the reference data. Because we abandon the SE assumption in this work, these components were not considered. We note that it is trivially possible to consider them also with the LNM by using the same SE assumption. For the GFM, alpha decaying nuclides are excluded if they do not contribute to the background in the ROI.

For components marked with \*, a considerable pile-up with their fast decaying daughter nuclide happens. As these pile-ups are excluded from the reference data, only the individual, not piled-up decays remain and can be fitted. Hence, the stated activities are only *lower limits* on the total activity of these components.

For all components, except those of the AER, the activity is given at the source of the background. For the AER components the activity is given as measured by the detector. Since the origin of the AER background is not known precisely, the specific source activity cannot be calculated.

Because the GFM uses upper limits from CUORE [44] for the copper contamination level, consequently only upper limits can be given for NER components.

<sup>7</sup>DuoPur, Milestone, Italy, <https://www.milestonesrl.com/products/clean-chemistry/subpur-and-duopur>

<sup>8</sup>AccuStandard, New Haven, USA, <https://www.accustandard.com>

<sup>9</sup>Triskem, France, [https://www.triskem-international.com/catalog/products/resins-and-accessories/tru-resin/bl\\_product,417,0](https://www.triskem-international.com/catalog/products/resins-and-accessories/tru-resin/bl_product,417,0)

<sup>10</sup>Element II, Thermo Fisher Scientific, USA, <https://www.thermofisher.com/order/catalog/product/IQLAEGAAMFABWMAFC>

<sup>11</sup><https://radiopurity.org>

Table 7: Results of the Gaussian fit method (GFM) and likelihood normalisation method (LNM) per background component in terms of contamination activities ( $A$ ). The results of the GFM in this work (see [Appendix A](#)) are updated with respect to the original results [13], see the text for details. The total uncertainty is the linear sum of statistical uncertainties (due to the sample statistic at 68 % C.L.) and systematic uncertainties (due to the normalisation values). Values are rounded to one significant digit on the uncertainty.

Background component	$(A \pm \delta_{\text{stat+sys}}) / \mu\text{Bq kg}^{-1}$	
	GFM	LNM
Internal Radiogenic (IR)		
$^{40}\text{K}$	–	< 0.01
$^{238}\text{U}$ chain		
$^{238}\text{U}$	$1070 \pm 30$	$1110 \pm 10$
$^{234}\text{Th}$	$1070 \pm 20$	$1260 \pm 20$
$^{234}\text{Pa}$	$1.70 \pm 0.03$	$1.7 \pm 0.2$
$^{234}\text{U}$	$1090 \pm 40$	$1150 \pm 10$
$^{230}\text{Th}$	$51 \pm 5$	$52 \pm 2$
$^{226}\text{Ra}$	$66 \pm 6$	$15 \pm 5$
$^{222}\text{Rn}$	$66 \pm 6$	$71 \pm 3$
$^{218}\text{Po}$	$66 \pm 6$	$60 \pm 3$
$^{214}\text{Pb}$	$66 \pm 5$	$71 \pm 9$
$^{218}\text{At}$	$0.013 \pm 0.001$	– <sup>a</sup>
$^{218}\text{Rn}$	– <sup>a</sup>	– <sup>a</sup>
$^{214}\text{Bi}$	$66 \pm 5$	< 0.01 <sup>*</sup>
$^{210}\text{Tl}$	$0.014 \pm 0.001$	$0.014 \pm 0.006$
$^{214}\text{Po}$	$66 \pm 5$	– <sup>b</sup>
$^{210}\text{Pb}$	$33 \pm 3$	$25 \pm 4$
$^{206}\text{Hg}$	$(63 \pm 5) \cdot 10^{-6}$	– <sup>a</sup>
$^{210}\text{Bi}$	$33 \pm 3$	$41 \pm 4$
$^{206}\text{Tl}$	$0.0044 \pm 0.0004$	– <sup>a</sup>
$^{210}\text{Po}$	$33 \pm 3$	$34 \pm 2$
$^{235}\text{U}$ chain		
$^{235}\text{U}$	$46 \pm 4$	$52 \pm 2$
$^{231}\text{Th}$	$46 \pm 3$	$99 \pm 4$
$^{231}\text{Pa}$	$45 \pm 4$	$49 \pm 2$
$^{227}\text{Ac}$	$144 \pm 5$	$184 \pm 6$
$^{223}\text{Fr}$	$1.98 \pm 0.07$	$2.0 \pm 0.2$
$^{227}\text{Th}$	$140 \pm 10$	$166 \pm 5$
$^{223}\text{Ra}$	$140 \pm 10$	$159 \pm 4$
$^{219}\text{At}$	$(124 \pm 4) \cdot 10^{-6}$	– <sup>a</sup>

*Continued on next page*

Table 7 - Continued from previous page

Component	$(A \pm \delta_{\text{stat+sys}}) / \mu\text{Bq kg}^{-1}$	
	GFM	LNМ
<sup>215</sup> Bi	$(113 \pm 4) \cdot 10^{-6}$	– <sup>a</sup>
<sup>219</sup> Rn	$135 \pm 6$	$0.2 \pm 0.2^*$
<sup>215</sup> Po	$135 \pm 6$	– <sup>b</sup>
<sup>211</sup> Pb	$135 \pm 6$	$180 \pm 10$
<sup>215</sup> At	$0.031 \pm 0.001$	– <sup>b</sup>
<sup>211</sup> Bi	$147 \pm 9$	$155 \pm 4$
<sup>207</sup> Tl	$147 \pm 6$	$180 \pm 10$
<sup>211</sup> Po	$0.41 \pm 0.02$	– <sup>b</sup>
<sup>232</sup> Th chain		
<sup>232</sup> Th	$11 \pm 2$	$10.8 \pm 0.9$
<sup>228</sup> Ra	$11 \pm 2$	$11 \pm 2$
<sup>228</sup> Ac	$11 \pm 2$	$8 \pm 2$
<sup>228</sup> Th	$25 \pm 4$	$30 \pm 2$
<sup>224</sup> Ra	$31 \pm 4$	$25 \pm 2$
<sup>220</sup> Rn	$13 \pm 2$	$8 \pm 1$
<sup>216</sup> Po	$13 \pm 2$	$< 0.01$
<sup>212</sup> Pb	$13 \pm 2$	$17 \pm 2$
<sup>212</sup> Bi	$13 \pm 2$	$23 \pm 5^*$
<sup>208</sup> Tl	$4.7 \pm 0.7$	$12 \pm 2$
<sup>212</sup> Po	$8 \pm 1$	– <sup>b</sup>
Near External Radiogenic (NER)		
<sup>40</sup> K	–	$< 0.01$
<sup>238</sup> U chain		
<sup>238</sup> U	–	– <sup>a</sup>
<sup>234</sup> Th	$< 123.88$	$< 0.01$
<sup>234</sup> Pa	$< 0.1982$	$0.1 \pm 0.1$
<sup>234</sup> U	–	– <sup>a</sup>
<sup>230</sup> Th	–	– <sup>a</sup>
<sup>226</sup> Ra	$< 123.9$	$< 0.01$
<sup>222</sup> Rn	–	– <sup>a</sup>
<sup>218</sup> Po	–	– <sup>a</sup>
<sup>214</sup> Pb	$< 123.9$	$6.2 \pm 0.1$
<sup>218</sup> At	$< 0.02478$	$< 0.01$

Continued on next page

Table 7 - Continued from previous page

Component	$(A \pm \delta_{\text{stat+sys}}) / \mu\text{Bq kg}^{-1}$	
	GFM	LMN
$^{218}\text{Rn}$	– <sup>a</sup>	– <sup>a</sup>
$^{214}\text{Bi}$	< 123.88	< 0.01
$^{210}\text{Tl}$	< 0.02602	< 0.01
$^{214}\text{Po}$	–	– <sup>a</sup>
$^{210}\text{Pb}$	< 123.88	$61 \pm 3$
$^{206}\text{Hg}$	< $2.354 \cdot 10^{-6}$	– <sup>a</sup>
$^{210}\text{Bi}$	< 123.88	$6.2 \pm 0.9$
$^{206}\text{Tl}$	< $1.6588 \cdot 10^{-4}$	– <sup>a</sup>
$^{210}\text{Po}$	–	– <sup>a</sup>
$^{235}\text{U}$ chain		
$^{235}\text{U}$	–	$0.04 \pm 0.04$
$^{231}\text{Th}$	< 0.8672	$0.04 \pm 0.02$
$^{231}\text{Pa}$	< 0.8672	$0.04 \pm 0.03$
$^{227}\text{Ac}$	–	– <sup>a</sup>
$^{223}\text{Fr}$	< 0.01197	< 0.01
$^{227}\text{Th}$	< 0.855	$0.04 \pm 0.04$
$^{223}\text{Ra}$	< 0.867	$0.04 \pm 0.03$
$^{219}\text{At}$	–	– <sup>a</sup>
$^{215}\text{Bi}$	< $6.721 \cdot 10^{-7}$	< 0.01
$^{219}\text{Rn}$	< 0.867	$0.04 \pm 0.04$
$^{215}\text{Po}$	–	– <sup>a</sup>
$^{211}\text{Pb}$	< 0.867	$0.04 \pm 0.02$
$^{215}\text{At}$	–	– <sup>a</sup>
$^{211}\text{Bi}$	< 0.8672	$0.04 \pm 0.04$
$^{207}\text{Tl}$	< 0.8648	$0.04 \pm 0.04$
$^{211}\text{Po}$	–	< 0.01
$^{232}\text{Th}$ chain		
$^{232}\text{Th}$	–	< 0.01
$^{228}\text{Ra}$	< 3.812	– <sup>a</sup>
$^{228}\text{Ac}$	< 3.812	< 0.01
$^{228}\text{Th}$	< 3.812	$2.0 \pm 0.2$
$^{224}\text{Ra}$	< 3.812	$2.00 \pm 0.06$
$^{220}\text{Rn}$	–	– <sup>a</sup>

Continued on next page

Table 7 - Continued from previous page

Component	$(A \pm \delta_{\text{stat+sys}}) / \mu\text{Bq kg}^{-1}$	
	GFM	LNM
$^{216}\text{Po}$	–	– <sup>a</sup>
$^{212}\text{Pb}$	< 3.812	< 0.01
$^{212}\text{Bi}$	< 3.812	< 0.01
$^{208}\text{Tl}$	< 1.370	< 0.01
$^{212}\text{Po}$	–	– <sup>a</sup>
Additional External Radiogenic (AER)		
$^{234}\text{Th}$	640 ± 20	1020 ± 30
$^{228}\text{Ra}$	–	< 0.01
$^{228}\text{Ac}$	1000 ± 100	365 ± 7
$^{226}\text{Ra}$	102 ± 3	58 ± 2
$^{214}\text{Bi}$	340 ± 30	204 ± 6
$^{212}\text{Bi}$	170 ± 40	260 ± 10
$^{212}\text{Pb}$	330 ± 20	124 ± 3
$^{210}\text{Pb}$	84 ± 3	< 0.01
$^{208}\text{Tl}$	580 ± 70	236 ± 5
$^{40}\text{K}$	220 ± 40	260 ± 10
Internal Cosmogenic (IC)		
$^{181}\text{W}$	39 ± 2	33 ± 3
$^{179}\text{Ta}$ (M <sub>1</sub> )	50 ± 2	45 ± 2
$^{179}\text{Ta}$ (M <sub>2</sub> )	–	12 ± 1
$^{179}\text{Ta}$ (M <sub>3</sub> )	–	2 ± 1
$^{179}\text{Ta}$ (L <sub>1</sub> )	136 ± 2	137 ± 3
$^{179}\text{Ta}$ (L <sub>2</sub> )	23 ± 1	19 ± 1
$^{179}\text{Ta}$ (L <sub>3</sub> )	–	< 0.01
$^{179}\text{Ta}$ (K)	177 ± 2	172 ± 3
$^3\text{H}$	24.2 ± 0.9	64 ± 4

<sup>a</sup> Strongly suppressed by branching ratio  $\leq 0.01\%$ .<sup>b</sup>  $Q$ -value of pure alpha decay beyond upper energy limit of the relevant reference data.

\* Significant amount of decays are excluded from the experimental data as pile-up events.

## References

- [1] J. Billard *et al.*, “Direct detection of dark matter—APPEC committee report,” *Reports on Progress in Physics*, vol. 85, no. 5, p. 056201, 2022. doi: [10.1088/1361-6633/ac5754](https://doi.org/10.1088/1361-6633/ac5754).
- [2] P. A. Zyla *et al.*, “Review of Particle Physics,” *PTEP*, vol. 2020, no. 8, p. 083C01, 2020. doi: [10.1093/ptep/ptaa104](https://doi.org/10.1093/ptep/ptaa104).
- [3] T. Jagemann *et al.*, “Measurement of nuclear recoil quenching factors in CaWO<sub>4</sub>,” *Astroparticle Physics*, vol. 26, no. 4, pp. 269–281, 2006, issn: 0927-6505. doi: [10.1016/j.astropartphys.2006.06.010](https://doi.org/10.1016/j.astropartphys.2006.06.010).
- [4] G. Jungman *et al.*, “Supersymmetric dark matter,” *Physics Reports*, vol. 267, no. 5, pp. 195–373, 1996. doi: [10.1016/0370-1573\(95\)00058-5](https://doi.org/10.1016/0370-1573(95)00058-5).
- [5] G. Angloher *et al.*, “Results on sub-GeV Dark Matter from a 10 eV Threshold CRESST-III Silicon Detector,” Dec. 2022. arXiv: [2212.12513](https://arxiv.org/abs/2212.12513) [[astro-ph.CO](https://arxiv.org/abs/2212.12513)].
- [6] H. Kluck *et al.*, “Latest results of CRESST-III’s search for sub-GeV/c<sup>-2</sup> dark matter,” *Journal of Physics: Conference Series*, vol. 1468, no. 1, p. 012038, 2020. doi: [10.1088/1742-6596/1468/1/012038](https://doi.org/10.1088/1742-6596/1468/1/012038).
- [7] G Angloher *et al.*, “Limits on wimp dark matter using sapphire cryogenic detectors,” *Astroparticle Physics*, vol. 18, no. 1, pp. 43–55, 2002. doi: [10.1016/S0927-6505\(02\)00111-1](https://doi.org/10.1016/S0927-6505(02)00111-1).
- [8] Angloher, G. *et al.*, “Probing spin-dependent dark matter interactions with <sup>6</sup>Li,” *Eur. Phys. J. C*, vol. 82, no. 3, p. 207, 2022. doi: [10.1140/epjc/s10052-022-10140-3](https://doi.org/10.1140/epjc/s10052-022-10140-3).
- [9] G. Angloher *et al.*, “Testing spin-dependent dark matter interactions with lithium aluminate targets in CRESST-III,” *Phys. Rev. D*, vol. 106, no. 9, p. 092008, 2022. doi: [10.1103/PhysRevD.106.092008](https://doi.org/10.1103/PhysRevD.106.092008). arXiv: [2207.07640](https://arxiv.org/abs/2207.07640) [[astro-ph.CO](https://arxiv.org/abs/2207.07640)].
- [10] S. Agostinelli *et al.*, “GEANT4—a simulation toolkit,” *Nuclear instruments and methods in physics research section A: Accelerators, Spectrometers, Detectors and Associated Equipment*, vol. 506, no. 3, pp. 250–303, 2003. doi: [10.1016/S0168-9002\(03\)01368-8](https://doi.org/10.1016/S0168-9002(03)01368-8).
- [11] J. Allison *et al.*, “Geant4 developments and applications,” *IEEE Trans. Nucl. Sci.*, vol. 53, no. 1, pp. 270–278, 2006. doi: [10.1109/TNS.2006.869826](https://doi.org/10.1109/TNS.2006.869826).
- [12] J. Allison *et al.*, “Recent developments in Geant4,” *Nucl. Instrum. Meth.*, vol. A835, pp. 186–225, 2016. doi: [10.1016/j.nima.2016.06.125](https://doi.org/10.1016/j.nima.2016.06.125).
- [13] A. H. Abdelhameed *et al.*, “Geant4-based electromagnetic background model for the CRESST dark matter experiment,” *Eur. Phys. J. C*, vol. 79, no. 10, p. 881, 2019, [Erratum: *Eur. Phys. J. C*, vol. 79, no. 12, p. 987, 2019. doi: [10.1140/epjc/s10052-019-7504-y](https://doi.org/10.1140/epjc/s10052-019-7504-y)]. doi: [10.1140/epjc/s10052-019-7385-0](https://doi.org/10.1140/epjc/s10052-019-7385-0). arXiv: [1908.06755](https://arxiv.org/abs/1908.06755) [[astro-ph.IM](https://arxiv.org/abs/1908.06755)].
- [14] P. Adari *et al.*, “EXCESS workshop: Descriptions of rising low-energy spectra,” *SciPost Phys. Proc.*, vol. 9, A. Fuss *et al.*, Eds., p. 001, 2022. doi: [10.21468/SciPostPhysProc.9.001](https://doi.org/10.21468/SciPostPhysProc.9.001). arXiv: [2202.05097](https://arxiv.org/abs/2202.05097) [[astro-ph.IM](https://arxiv.org/abs/2202.05097)].
- [15] G. Angloher *et al.*, “Latest observations on the low energy excess in CRESST-III,” in *14th International Workshop on the Identification of Dark Matter 2022*, Jul. 2022. arXiv: [2207.09375](https://arxiv.org/abs/2207.09375) [[astro-ph.CO](https://arxiv.org/abs/2207.09375)].
- [16] H. Kluck, “ELOISE - Reliable background simulation at sub-keV energies,” in *14th International Conference on Identification of Dark Matter (IDM2022)*, 2023, p. 064. doi: [10.21468/SciPostPhysProc.12.064](https://doi.org/10.21468/SciPostPhysProc.12.064). arXiv: [2212.12634](https://arxiv.org/abs/2212.12634) [[physics.ins-det](https://arxiv.org/abs/2212.12634)].
- [17] M. F. L’Annunziata, *Handbook of radioactivity analysis*. Academic press, 2020. doi: [10.1016/C2016-0-04811-8](https://doi.org/10.1016/C2016-0-04811-8).
- [18] F. Danevich *et al.*, “Effect of recrystallisation on the radioactive contamination of CaWO<sub>4</sub> crystal scintillators,” *Nuclear Instruments and Methods in Physics Research Section A: Accelerators, Spectrometers, Detectors and Associated Equipment*, vol. 631, no. 1, pp. 44–53, 2011. doi: [10.1016/j.nima.2010.11.118](https://doi.org/10.1016/j.nima.2010.11.118).
- [19] F. A. Danevich *et al.*, “Radioactive contamination of scintillators,” *International Journal of Modern Physics A*, vol. 33, no. 09, p. 1843007, Mar. 2018. doi: [10.1142/s0217751x18430078](https://doi.org/10.1142/s0217751x18430078).
- [20] A. Fuß, “Simulation based Neutron Background Studies for the CRESST and COSINUS Dark Matter Search Experiments,” Ph.D. dissertation, 2022. doi: [10.34726/HSS.2022.86617](https://doi.org/10.34726/HSS.2022.86617).
- [21] G. Angloher *et al.*, “Secular equilibrium assessment in a CaWO<sub>4</sub> target crystal from the dark matter experiment CRESST using Bayesian likelihood normalisation,” *Appl. Radiat. Isot.*, vol. 194, p. 110670, 2023. doi: [10.1016/j.apradiso.2023.110670](https://doi.org/10.1016/j.apradiso.2023.110670). arXiv: [2209.00461](https://arxiv.org/abs/2209.00461) [[physics.ins-det](https://arxiv.org/abs/2209.00461)].
- [22] G Angloher *et al.*, “Results on low mass WIMPs using an upgraded CRESST-II detector,” *The European Physical Journal C*, vol. 74, no. 12, pp. 1–6, 2014. doi: [10.1140/epjc/s10052-014-3184-9](https://doi.org/10.1140/epjc/s10052-014-3184-9).
- [23] R Strauss *et al.*, “Beta/gamma and alpha backgrounds in CRESST-II phase 2,” *Journal of Cosmology and Astroparticle Physics*, vol. 2015, no. 06, p. 030, 2015. doi: [10.1088/1475-7516/2015/06/030](https://doi.org/10.1088/1475-7516/2015/06/030).
- [24] M. Stahlberg, “Probing low-mass dark matter with cressst-iii: Data analysis and first results,” Ph.D. dissertation, Wien, 2020.
- [25] J. W. Beeman *et al.*, “Radiopurity of a kg-scale PbWO<sub>4</sub> cryogenic detector produced from archaeolog-

- ical Pb for the RES-NOVA experiment,” *The European Physical Journal C*, vol. 82, no. 8, Aug. 2022. doi: [10.1140/epjc/s10052-022-10656-8](https://doi.org/10.1140/epjc/s10052-022-10656-8).
- [26] A. Aguilar-Arevalo *et al.*, “Characterization of the background spectrum in DAMIC at SNOLAB,” 2021. arXiv: [2110.13133 \[hep-ex\]](https://arxiv.org/abs/2110.13133).
- [27] G. Adhikari *et al.*, “Strong constraints from COSINE-100 on the DAMA dark matter results using the same sodium iodide target,” *Science Advances*, vol. 7, no. 46, eabk2699, 2021. doi: [10.1126/sciadv.abk2699](https://doi.org/10.1126/sciadv.abk2699).
- [28] C. Türkoğlu, “Development of a Geant4 based electromagnetic background model for the CRESST experiment,” Ph.D. dissertation, Wien, 2018.
- [29] A. Caldwell *et al.*, “BAT manual 1.0.0,” Accessed: 30.09.2021. [Online]. Available: <https://bat.github.io/bat-docs/master/manual/BAT-manual.pdf>.
- [30] H. H. Ku *et al.*, “Notes on the use of propagation of error formulas,” *Journal of Research of the National Bureau of Standards*, vol. 70, no. 4, pp. 263–273, 1966. doi: [10.6028/jres.070C.025](https://doi.org/10.6028/jres.070C.025).
- [31] J. Burkhart, “Enhancing the Electromagnetic Background Model of CRESST-II,” M.S. thesis, Technische Universität Wien, 2022. doi: [10.34726/hss.2022.104928](https://doi.org/10.34726/hss.2022.104928).
- [32] G. Cowan, *Statistical data analysis*. Oxford university press, 1998.
- [33] A. Caldwell *et al.*, “BAT—the Bayesian analysis toolkit,” *Computer Physics Communications*, vol. 180, no. 11, pp. 2197–2209, 2009. doi: [10.1016/j.cpc.2009.06.026](https://doi.org/10.1016/j.cpc.2009.06.026).
- [34] C. P. Robert *et al.*, *Monte Carlo statistical methods*. Springer, 2004, vol. 2. doi: [10.1007/978-1-4757-4145-2](https://doi.org/10.1007/978-1-4757-4145-2).
- [35] W. K. Hastings, “Monte Carlo sampling methods using Markov chains and their applications,” *Biometrika*, vol. 57, no. 1, pp. 97–109, 1970. doi: [10.2307/2334940](https://doi.org/10.2307/2334940).
- [36] N. Metropolis *et al.*, “Equation of state calculations by fast computing machines,” *The journal of chemical physics*, vol. 21, no. 6, pp. 1087–1092, 1953. doi: [10.1063/1.1699114](https://doi.org/10.1063/1.1699114).
- [37] S. Brooks *et al.*, *Handbook of Markov chain Monte Carlo*. CRC press, 2011. doi: [10.1201/b10905](https://doi.org/10.1201/b10905).
- [38] S. Chib *et al.*, “Understanding the Metropolis-Hastings Algorithm,” *The American Statistician*, vol. 49, no. 4, pp. 327–335, 1995. doi: [10.1080/00031305.1995.10476177](https://doi.org/10.1080/00031305.1995.10476177).
- [39] S. Kirkpatrick *et al.*, “Optimization by simulated annealing,” *science*, vol. 220, no. 4598, pp. 671–680, 1983. doi: [10.1126/science.220.4598.671](https://doi.org/10.1126/science.220.4598.671).
- [40] F. James *et al.*, “Minuit - a system for function minimization and analysis of the parameter errors and correlations,” *Computer Physics Communications*, vol. 10, no. 6, pp. 343–367, 1975. doi: [10.1016/0010-4655\(75\)90039-9](https://doi.org/10.1016/0010-4655(75)90039-9).
- [41] A. Gelman *et al.*, “Inference from iterative simulation using multiple sequences,” *Statistical science*, vol. 7, no. 4, pp. 457–472, 1992. doi: [10.1214/ss/1177011136](https://doi.org/10.1214/ss/1177011136).
- [42] M. P. Fay, “Two-sided exact tests and matching confidence intervals for discrete data,” *R Journal*, vol. 2, no. 1, p. 53, 2010. doi: [10.32614/RJ-2010-008](https://doi.org/10.32614/RJ-2010-008).
- [43] K. F. Hirji, *Exact analysis of discrete data*. Chapman and Hall/CRC, 2005. doi: [10.1201/9781420036190](https://doi.org/10.1201/9781420036190).
- [44] C. Alduino *et al.*, “CUORE-0 detector: Design, construction and operation,” *Journal of Instrumentation*, vol. 11, no. 07, P07009, 2016. doi: [10.1088/1748-0221/11/07/P07009](https://doi.org/10.1088/1748-0221/11/07/P07009).
- [45] H. Kluck *et al.*, “Cosmic activation of CRESST’s CaWO<sub>4</sub> crystals,” *J. Phys. Conf. Ser.*, vol. 2156, p. 012227, 2021. doi: [10.1088/1742-6596/2156/1/012227](https://doi.org/10.1088/1742-6596/2156/1/012227).
- [46] J. Back *et al.*, “ACTIVIA: Calculation of isotope production cross-sections and yields,” *Nuclear Instruments and Methods in Physics Research Section A: Accelerators, Spectrometers, Detectors and Associated Equipment*, vol. 586, no. 2, pp. 286–294, 2008. doi: [10.1016/j.nima.2007.12.008](https://doi.org/10.1016/j.nima.2007.12.008).
- [47] C. Arpesella, “A low background counting facility at laboratori nazionali del Gran Sasso,” *Applied Radiation and Isotopes*, vol. 47, no. 9, pp. 991–996, 1996. doi: [10.1016/S0969-8043\(96\)00097-8](https://doi.org/10.1016/S0969-8043(96)00097-8).
- [48] M. Laubenstein, “Screening of materials with high purity germanium detectors at the Laboratori Nazionali del Gran Sasso,” *Int. J. Mod. Phys. A*, vol. 32, no. 30, p. 1743002, 2017. doi: [10.1142/S0217751X17430023](https://doi.org/10.1142/S0217751X17430023).
- [49] H. Neder *et al.*, “Low level  $\gamma$ -ray germanium-spectrometer to measure very low primordial radionuclide concentrations,” *Applied Radiation and Isotopes*, no. 1, pp. 191–195, doi: [10.1016/S0969-8043\(00\)00132-9](https://doi.org/10.1016/S0969-8043(00)00132-9).
- [50] G. Heusser *et al.*, “Low-level germanium gamma-ray spectrometry at the  $\mu\text{Bq/kg}$  level and future developments towards higher sensitivity,” in *Radionuclides in the Environment*, ser. Radioactivity in the Environment, P. Povinec *et al.*, Eds., Elsevier, pp. 495–510. doi: [10.1016/S1569-4860\(05\)08039-3](https://doi.org/10.1016/S1569-4860(05)08039-3).
- [51] G. Rugel *et al.*, “A Germanium spectrometer for routine characterisation of samples with the sensitivity of  $\beta\beta$ -decay spectrometers,” *Nucl. Phys. B Proc. Suppl.*, vol. 143, J. Dumarchez *et al.*, Eds., pp. 564–564, 2005. doi: [10.1016/j.nuclphysbps.2005.01.228](https://doi.org/10.1016/j.nuclphysbps.2005.01.228).